Topics in Calorimetry for High Energy Physics

Robert Hollebeek
University of Pennsylvania

1991 SLAC Summer School Lectures

1 Introduction

These lectures were given at the 1991 SLAC Summer Institute for Particle Physics where my assignment was to speak about Calorimetry in High Energy Physics. This is actually an impossibly broad topic for only three lectures, so I needed to make some choices. Calorimeters come in many different varieties, and are used in almost all high energy physics experiments either as detectors or targets. These lectures were not intended to be a reference on the details of electromagnetic or hadronic interactions within calorimeters, nor were they meant to be a catalog of the latest in detector techniques. The former would be too detailed to be useful for most experimentalists, and the latter would be too soon obsolete. Many new experiments are at the planning stage at the moment for the SSC, the LHC, and future fixed target, collider and eeB factories, with many calorimeter choices and design details remaining to be made. A great deal of effort is going into test beams as well, for which the data is not yet available. Therefore, I have chosen to focus on a series of topics which are now of interest, or have been of interest to designers of calorimeters in the past few years in the hopes that the students at the institute can become aware of some of the current issues in the field and can hopefully avoid some of the mistakes of the past should they ever be called upon to design one of their own. For examples, I have concentrated on calorimeters from DESY because the focus of the institute this year is eP physics, and on CDF and SDC because those are the calorimeters which are the most familiar to me.

Calorimeters are, broadly speaking, devices to measure the total energy of particles. Various techniques can therefore be applied, depending on the detailed properties of the particles of interest, and in general, no one device will be optimal for all types of particles. The two broadest subclasses of calorimeters in high energy physics are the electromagnetic calorimeters used primarily for photons and electrons, and the hadronic calorimeters used for most charged mesons and baryons. Most of these types of calorimeters operate by absorbing and thereby measuring a significant amount of the incoming particle's energy directly. A few particles represent particularly difficult cases where this may not be possible, and therefore may require special devices. In this case, I am thinking of muons where the total energy may be measured by tracking or by range, neutrinos, where the technique may involve the kinematics of a particular low energy reaction or the use of missing energy techniques, or jets where corrections need to be applied for the types of particles in the jet, their energy spectra, and perhaps charged to neutral ratios. These latter cases represent more complicated applications of the calorimeter technique together with the gathering of other information. Even in these cases, the performance of the calorimeter will be determined primarily by its energy and position resolution. Another characteristic of the calorimeter which has become increasingly important in recent years is its cost. As the energies of interest have increased over the years, so has the size of the calorimeter. Its cost can represent a significant fraction of the total cost of an apparatus, and thus it may be necessary to carefully determine the trade-off between performance and cost.

When optimizing the resolution, one must be clear to define when enough is enough. This should in principle be done by using benchmark physics processes to estimate the required performance of the detector as a whole and its dependence on the calorimeter, keeping in mind however that for those experiments which will be probing a new energy range or a new set of phenomena, that the requirements are rarely well known in advance, and so it may be wise to plan on somewhat more ability in the detector than is obviously required from simulations based only on the currently known physics processes. The resolution will be affected by the overall thickness of the detector, by the choice of uniform or sampling techniques, by sampling fluctuations, and by variations in the calibration either as a function of time, or throughout the volume of the calorimeter. The optimum cost will require a careful choice of materials, reduction of the overall size of the detector, elimination of labor intensive construction techniques,and careful consideration of the cost of calibration systems. Since at least some of these requirements which optimize cost and resolution are contradictory, the ideal calorimeter is seldom what one ends up building, and coming as close as possible can be a difficult venture.

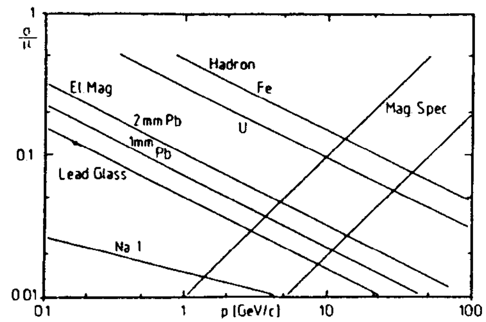

Figure 1: A comparison of the resolution of calorimeters and magnetic spectrometers as a function of energy.

1.1 Why Bother?

Calorimetry has two major nice features. First, the depth of the device required to contain a fixed percentage of an incoming particle's energy scales as lnE, and second, the resolution of the detector improves with energy. As the energy scale of the machines which we build increases, the maximum interesting energy scales of course like E, and the mean particle energy scales roughly as ln E. In these cases, the resolution of the calorimeter will improve like 1/E or at least 1/ ln E. The importance of this gradual increase in the performance of the calorimeter is shown in figure 1. Electromagnetic and hadronic calorimeter resolutions improve with energy while tracking detectors degrade. Figure 1 shows that in the range of a few tens of GeV, even hadron calorimeters have a better resolution than a tracking detector.

The performance of calorimeters as a function of energy is also well matched to the eventual transition from concentrating on the reconstruction of exclusive final states which is a powerful technique at low energies, to the use of groups of particles (jets) as pseudo-particles in an analysis. Calorimeters with reasonable segmentation are often not very good at separating particles which are close together, but they can still measure the energy of the "jet" well, provided the calorimeter has reasonable linearity.

2 Resolution

The achievable resolution of the calorimeter depends primarily on the statistics of the underlying process, and hence is quite different for electromagnetic devices where a large number of particles contribute to the shower, and the hadronic device where the number of such particles is fewer because of higher thresholds for particle production. Some representative values of the performance of various types of electromagnetic calorimeters are (where the range represents changes since about 1984)

NaI - Crystal Ball

$$\sigma = \frac{2.7\%}{\mathrm{E}^{1/4}}$$

Lead Glass (OPAL)

$$\sigma = \frac{5-12\%}{\sqrt{\mathrm{E}}}$$

Lead - Liquid Argon (NA31)

$$\sigma = \frac{7.5-16\%}{\sqrt{\mathrm{E}}}$$

Lead - Scintillator (ARGUS)

$$\sigma = \frac{9-17\%}{\sqrt{\mathrm{E}}}$$

Lead - PWC (MAC)

$$\sigma = \frac{23-40\%}{\sqrt{\mathrm{E}}}$$

Spaghetti - CERN Spacal

$$\sigma = \frac{13\%}{\sqrt{\mathrm{E}}}$$

Hadronic calorimeters have resolutions which are more typically $35\%/\sqrt{E}$. This more limited resolution comes about both because of the higher intrinsic minimum energy required for a shower compared to an electromagnetic shower, and because there are several different processes which contribute to a hadronic shower with different sensitivities, and fluctuations in the fractional energy deposition due to these different processes will contribute to the degradation of the resolution.

3 Hadron Calorimeters

A hadronic shower contains both a hadronic component due primarily to $\pi^{\pm}$ production, as well as an electromagnetic component due primarily to the production of π^0. Thus a difference in the detected energy response for these two components will result in poor overall resolution when the fraction of neutral and charged pions fluctuates.

Figure 2 shows the ratio of average energy deposited for electrons and hadrons as a function of energy for several different types of calorimeters. At 10 GeV, the resolution achieved was 50% for Iron Scintillator, 28% for Iron Scintillator with three times finer sampling (indicating the relative importance of sampling fluctuations), 25% for Iron using either PWC or Scintillator readout, 19% for very finely segmented Iron and liquid Argon, and finally 12% for Uranium-Copper-Scintillator. These resolutions are therefore best for calorimeter materials with electron to hadron ratios close to one.

Before trying to explain the principles of calorimetry further, it is best to discuss a few examples of current calorimeters. The Zeus hadron calorimeter will be used as an example here. It is projective in ϕ but not in θ. Signals from the scintillator are read by using a wavelength shifter technique, and provision is made for two gaps where silicon detectors can be used to sample the shape of the shower at a depth of 3 and 6 X_0 in the electromagnetic section. The calorimeter is constructed on a C shaped frame as shown in Figure 3 made from steel plate welded into a box beam.

3.1 The Wavelength Shifters

In the ZEUS forward and rear calorimeters, as in most calorimeters, it is difficult mechanically to pipe the light from the scintillator to the phototube. One method

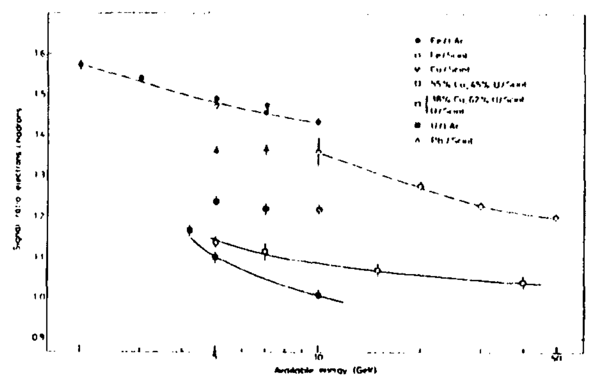

Figure 2: The signal ratio for electrons and hadrons, and its effect on resolution achieved for Iron Scintillator, Iron Liquid Argon, Lead Scintillator and Uranium-Copper Calorimeters.

which works well is to have the light strike another material which will reradiate isotropically and this reradiation can be used to get the light to effectively make a right angle turn at the side of a module in order to head toward the rear of the module where the phototubes are situated. There are problems with this technique, however. For example, often the reradiator is made of BBQ, a material which has an absorption peak in the far blue (380nm) where there is, however, reduced scintillation light, and reradiates in a range (500 nm) beyond the sensitivity of most phototubes. (Some improvement can be had with PLEXIPOP which has an emission peak at 410 um.)

An additional problem involves the time structure of the pulse. Reradiation can be a slow process (with time constants of order 15 ns) and therefore one must be careful to choose a fast fluor for a detector which must have good time resolution. As shown in Figure 4, an air gap is required between the sampling sheets of scintillator and the wavelength shifter plate. The gap is often maintained with a nylon thread. Finally, the wavebars have reflectors at the end opposite the phototube in order to increase the light yield.

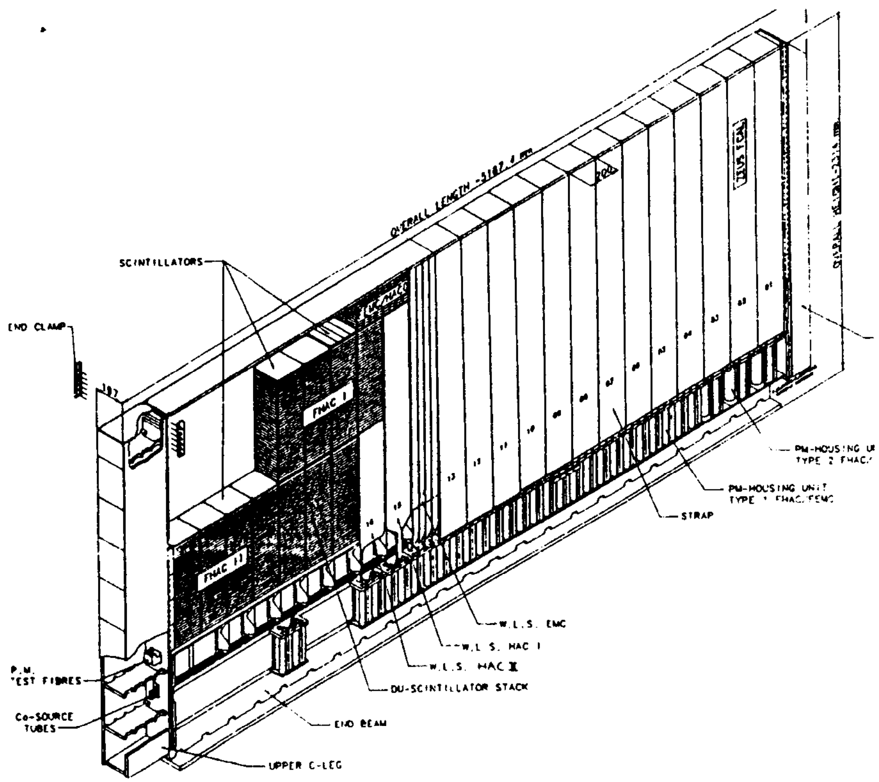

Figure 3: The ZEUS Calorimeter constructed on a welded box beam C frame.

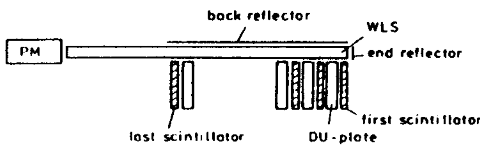

Figure 4: Wavelength shifters use an air gap and the isotropic re-radiation of light in the WLS to re-direct light to the phototube.

3.2 Construction Details

Because Uranium provides a better electron to hadron ratio, and therefore better resolution, the Zeus calorimeter is made of Uranium plates. The Uranium plate thickness is $1X_0$. The plate is made from depleted Uranium. (98.1% U, 1.7% Nb, < 0.2 % U (235)), and is 3.3 mm thick. Pure Uranium 238 would have a radiation length of 3.2 mm and an absorption length of 10.5 cm. The plates are encapsulated in stainless both to minimize the safety problems involved in handling the plates and to adjust the rate of the natural Uranium radioactivity used as a calibration source. The rate needs to be high enough to allow calibration in a reasonable amount of time, but it needs to be small enough so that these random pulses do not make a large contribution to the calorimeter noise. The stainless thickness is 0.2 mm for the EM part of the calorimeter, and 0.4 mm for the hadronic part.

The scintillator thickness is adjusted, as will be discussed later, to provide $e/h = 1$, that is, the same response on average for both electromagnetic and hadronic showers in the hadron calorimeter. The thickness is 2.6 mm. Since any mechanical pressure on the surface of the plastic scintillator can cause surface degradation and therefore loss of light, the Uranium plates must be self supporting, providing shelves for holding the plastic. This is accomplished by placing spacers between the Uranium plates. Different size spacers (3.8 mm, 3.9 mm, 4.0 mm) are used to adjust the overall size of the stack. Every 25 plates during construction, the stack is measured and compressed and skimmed with the spacers. (See Figure 5.) Final tensioning of the full stack gives a compression of 3 mm.

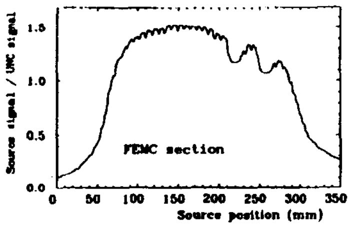

Figure 5: Response scan thru an electromagnetic section. The two large dips are due to gaps left for silicon detectors.

3.3 Optical Response

The optical response of the calorimeter depends on the light yield and uniformity of the plastic which in this case is SCSN-38 cast polystyrene. Individual plates are cast with a ±0.2 mm tolerance on the thickness (10%) pulse height variation and the attenuation length of each plate is measured. Information on the plates is collected, and computerized sorting of the plates is used to improve the overall uniformity of completed modules. The particular choice of SCSN-38 is motivated by its fast fluor (short decay time), its radiation hardness (the machine produces 100 Gy/year while the Uranium itself contributes 10 Gy/year), and its cheaper cost.

Figure 5 shows a source scan through the depth of a forward electromagnetic section. Individual plates can be seen as well as the two gaps left for silicon sampling. Figure 6 shows the results of radiation damage studies on a module. The plot shows the attenuation length as a function of time after irradiation. Note that with 14.3 Gy, there is little difference between irradiated and non-irradiated samples. With a larger dose of 52 Gy, there is an initial loss in light output, but the gradual change in attenuation length with time is slowed in the irradiated sample.

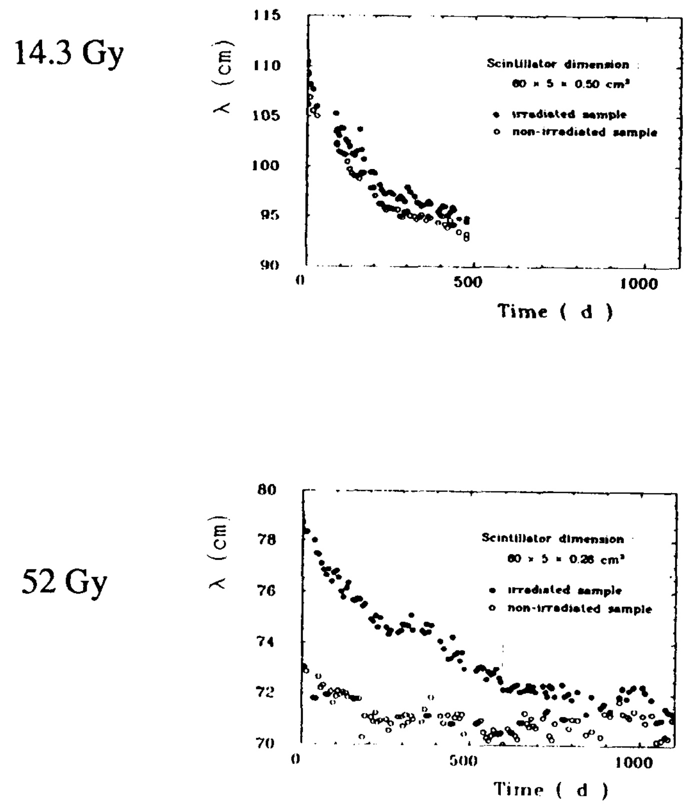

Figure 6: Radiation damage studies.

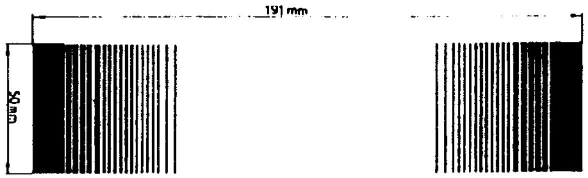

Figure 7: Masking pattern applied to the surface to correct for attenuation.

3.4 Masking Patterns and Uniformity

Since blue light usually has a shorter attenuation length than red light due to absorption in the scintillator, the total light output seen by a phototube generally increases as a source approaches the end of a stack. This effect would lead to a variation in energy response across the face of a module which needs to be corrected. The total light yield can be changed by varying the reflectivity of the surface of the scintillator and this correction can be adjusted to compensate for the above effect.

Figure 7 shows a typical masking pattern applied to the surface of a plate in order to correct for attenuation. Figure 8 shows a typical light yield curve with and without the correction. Individual masking patterns need to be calculated based on the measured attenuation length of each sheet for best results. The resulting mask can be printed on a Laser printer.

3.5 Birk's Law

[1] As mentioned previously, to optimize the calorimeter resolution, the average response to electromagnetic and hadronic showers must be the same. In 1951, Birk published a study of the loss of signal from α particles where he found that the loss of signal depended on the number of α's which had hit the crystal. There was obvious brown discoloration on the surface, but the effect was more than just optical absorption. His hypothesis was that each α damages a number of molecules (p) so that the concentration of undamaged molecules goes like

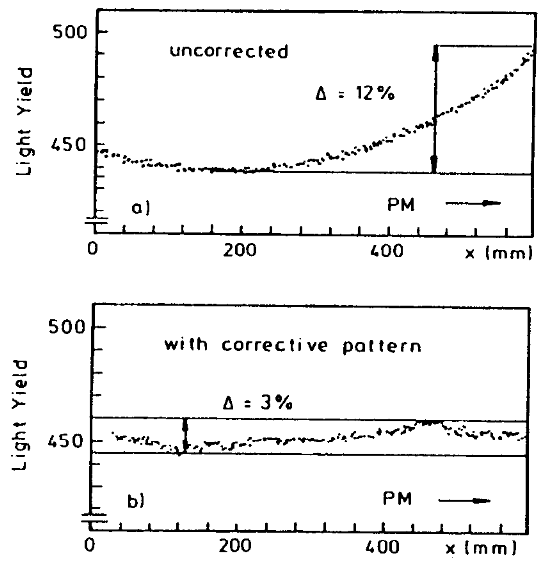

Figure 8: Light yield as a function of distance from the front of the module with and without masking corrections.

$$x = \exp\left(\frac{pN}{q_0}\right) - 1$$

where q_0 is the original concentration, and N is the number of α's. If k is the absorption probability of one of these molecules, the light output will be

$$\frac{I}{I_0} = \frac{1}{1 + kx} \quad .$$

The modern statement of Birk's law which describes such a situation is

$$\frac{dL}{dx} \sim \frac{dE}{dx}\left(\frac{1}{1 + k_B \frac{dE}{dx}}\right).$$

In the modern context, the light yield from the scintillator depends on the ionization loss dE/dx with heavily ionizing particles leaving reduced yield. This effect may result from damage produced locally near the ionization trail. The damage may, of course, be reversible even on a very short time scale. In warm liquid replacements for liquid Argon, for example, the reduction in output for heavy ionization occurs when positive ions recombine with electrons near the dense ion trail before the electrons travel far enough away to be free. This effect is reversible. Reduction in output due to damage produced in the medium is generally not reversible.

3.6 Calibration

The Uranium in the ZEUS calorimeters can be used as a calibration source. The decay lifetime of Uranium is 4.5 10^9 years and therefore makes a very stable reference. The natural radiation consists of α β, and γ radiation. The α's carry 80% of the total energy but have very short range, and most of this energy is absorbed in the Uranium or in the stainless cladding material. The β's carry most of the rest of the energy with a spectrum extending to 2.3 MeV which gives a 1 mm range in Uranium. One percent of the energy is in the form of γ's with energies ranging from 10 keV to 1 MeV.

Measurements of radiation at the surface of Uranium plates give 2600 β decays per square cm with an average energy of 200 keV and 442 γ's with an average energy of 500 keV. These rates are reduced 70% by the stainless cladding used in

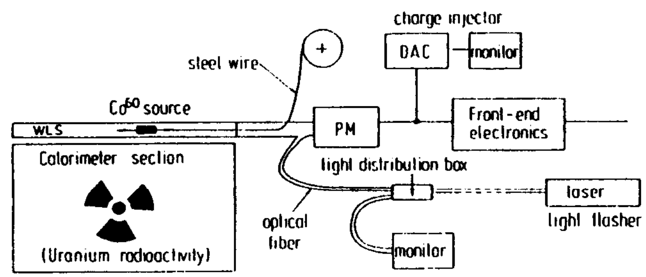

Figure 9: A typical calibration system (ZEUS) uses radioactive sources, light flashers, and charge injectors.

EM modules, and 90% by the hadron calorimeter cladding (which is thicker). This natural radioactivity makes a useful monitor of the overall calibration stability of a module once it is constructed. In all good calorimeters, however, it is wise to include as many calibration sources and checks as possible. In the ZEUS case, there are 2 mCI Cobalt 60 sources on motor driven wires which can travel on fixed paths inside the modules of the calorimeter, light flashers using a nitrogen dye laser test the phototubes, and charge injectors used for the electronics calibration. (See Figure 9.)

3.7 Electronics

Due to the 96 ns time between bunches at HERA, the electronics must be able to pipeline and store the data from each crossing during the 5μs processing time for the trigger. The electronics [2] has a very impressive dynamic range of 16.5 bits and can thus measure over the full range from 300 MeV (which is a mip-minimum ionizing particle equivalent) to the maximum energy of 400 GEV with full resolution. This is accomplished by having two signal channels, one with high gain, and a second with gain reduced by a factor of 22.22. Data is recorded by 12 bit 1MHz ADC's which feed into a 58 cell pipeline. There is also a trigger circuit, and a DC calibration circuit with integration time of 20 ms for the Uranium pulses. This calibration circuit has a precision of 1%. The high gain circuit gives 8 samples per pulse and provides a timing accuracy of a few ns. (See Figure 10.)

3.8 Test Beams

After construction of a calorimeter module, and design and construction of the associated electronics, the detector must be tested and calibrated in a test beam. Figures 11 and 12 show the results for the ZEUS forward and rear calorimeters respectively. The resolution is about 17% with an expected contribution (in quadrature) of 1% from the beam, and 16% from sampling fluctuations, and a small contribution from photostatistics. In general, a deviation from linearity indicates a problem and, at the time of the lectures, the non-linearity in the RCAL was unexplained.

It is also important to obtain information from the test beam about the uniformity of response across a module so that this information can be used later as a correction. This is particularly true of the electromagnetic section because the electromagnetic showers (which are smaller than the hadronic showers) will be more sensitive to small scale nonuniformities in the construction of the module. Figure 13 shows such a scan for the FCAL and RCAL. The dips every 5 cm are caused by the 0.5 mm gap between modules. There is a 10% drop in the electron signal at these locations. There is also a 7% loss at the position of the spacers used to separate the Uranium plates.

The magnitude of the dip seen as one scans across such dead spots depends crucially on the size of the scanning beam which must in general be smaller than the electron shower size. In the same way, when test beam data is used to correct the energy response of a shower in the final detector, the ability to apply the correction will depend on the ability of the rest of the apparatus (tracking chambers, etc.) to determine the impact point and angle of an incoming track.

Figure 14 shows the achieved resolution for both hadrons and electrons and the ratio of the e and h responses as a function of energy. The achieved resolution for hadrons of $35\%/\sqrt{E}$ is excellent for a hadron calorimeter.

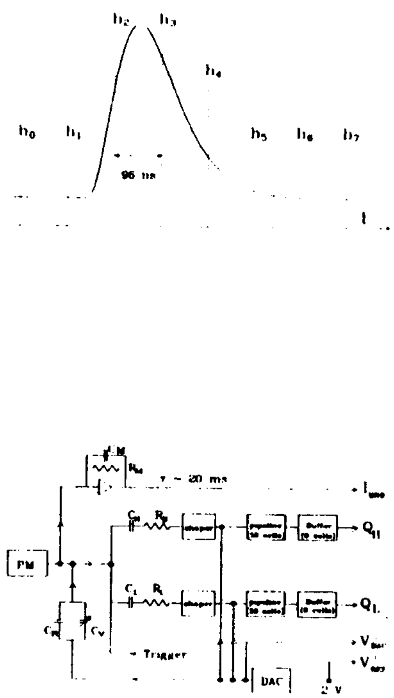

Figure 10: Electronics (ZEUS) with a high and low gain channel for increased dynamic range, and a slow channel for source calibration. Each pulse is measured at 8 times.

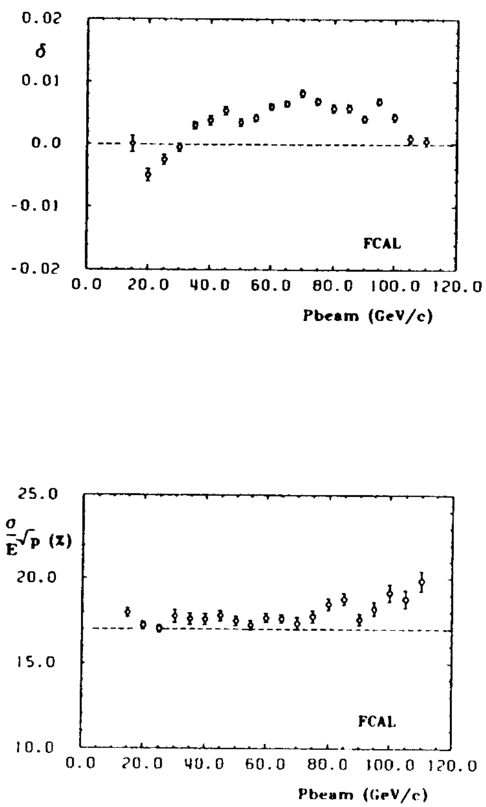

Figure 11: Deviation from linearity and resolution for the ZEUS FCAL from test beam results.

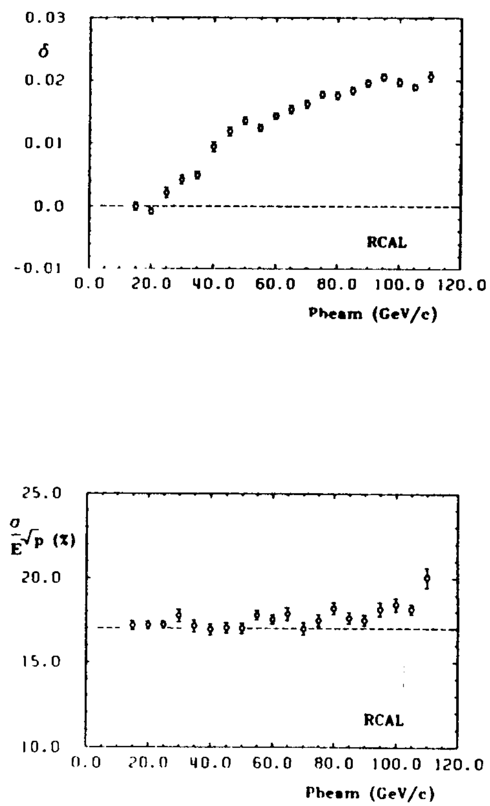

Figure 12: Deviation from linearity and resolution for the ZEUS RCAL from test beam results.

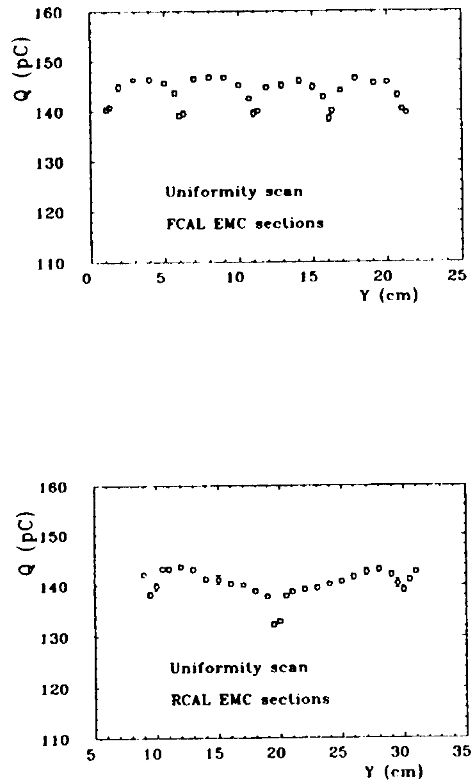

Figure 13: Uniformity scans for RCAL and FCAL electromagnetic sections.

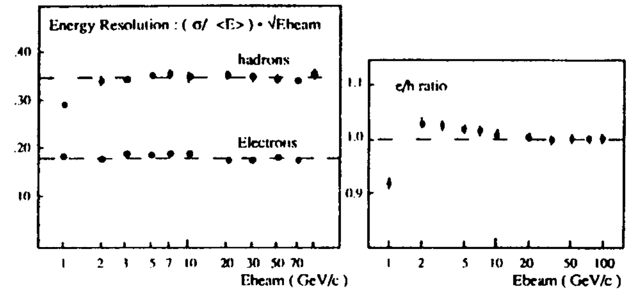

Figure 14: Resolution and e/h ratio for hadrons and electrons as a function of energy.

4 SDC - Scintillating Tile and Fiber

In one of the designs being considered for the SDC detector, the calorimeter is constructed from small plates or "tiles" in which optical fibers have been imbedded. See Figure 14. The optical fibers are doped with wave shifter and capture about 4% of the blue scintillation light.

Some of the advantages of this technique include low cost, a small "constant term" in the resolution if compensation can be achieved, easy transverse and longitudinal segmentation, and smaller inter-module spacing relative to the use of wavebar readout because of the relative size of fibers versus other light guides (0.5% vs. several percent losses due to inter-module cracks). Some of the difficulties of this technique are that it requires more mechanical work than wave-bars, for example, grooving the plates, imbedding the wave shifter fiber, joining the wave shifter fiber to clear fiber at the plate edge (to avoid large signals from showers in a fiber bundle bringing signals out of a module), and somewhat more difficulty in achieving uniformity across a module (masking plates in this configuration would be complex).

One to two percent uniformity has been achieved across an individual tile, and given the large number of tiles involved in a single shower, this may be sufficient. The absolute light yield of this configuration is about 4 times that of a wave bar.

This is due to better coupling of light to the fibers than is achieved with air gaps and wave bars, longer attenuation lengths in fibers than in wave bars, and shorter light paths in the scintillator. The small optical collection region for light leads to a timing resolution dominated by the decay time of the wave shifter which can be as short as 3 - 10 ns, for example, with some green dyes. Radiation hardness may be improved relative to wave bars because the path lengths for blue light in such a device are short (just the shower to nearest fiber distance) and radiation damage usually affects shorter wavelengths more.

The large number of individual tiles required for a full calorimeter and the large number of individual steps required for each tile means that considerable effort has to go into automation procedures. Areas where this is being studied include laser cutting the tiles, milling the grooves, glue injection into the groove, painting the sides of tiles with reflective paint, splicing readout fibers, calculating masking patterns, wrapping the tile with the flattening mask, and stacking finished tiles and absorbers.

The absorber materials which have been considered for this design have been Uranium, Lead, and Iron. The obvious advantage of Iron is that it can double as a flux return; the serious disadvantage is that it leads to low hadronic response due to a small neutron yield. Uranium is good, but difficult to machine and handle, expensive and perhaps difficult to obtain in sufficiently large quantities. Lead represents somewhat of a compromise. A 2:1 ratio of lead to scintillator would give e/h of order 1.1 and a calorimeter where the constant term in the resolution begins to dominate above 100 GeV.

The relative neutron yields of U:Pb:Fe are 5:2:1. The calorimetric yields are unknown but presumably similar. Since neutron response can lead to a slow tail on the time structure of a hadron shower, it may be that Lead and Iron calorimeters are intrinsically faster devices. The compensating ($e/h \approx 1$) ratio of Fe: Scintillator thickness is, however, estimated to be as high as 10:1 which would lead to unacceptably large sample fluctuations. Compensation in Iron basically works by suppression of the EM component. Perhaps small amounts of Lead can be added to Iron to improve the thickness ratio requirement. Finally, with Iron, the possibility exists of making the absorber out of stamped laminations which are then assembled together to provide holes for the tiles.

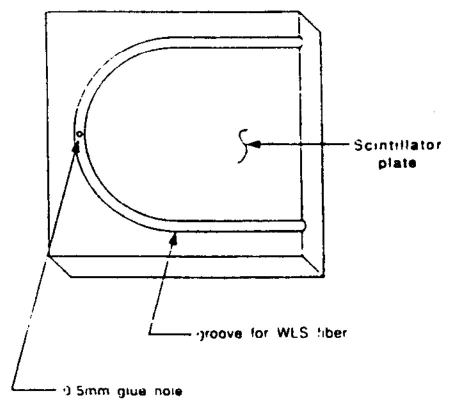

Figure 15: Scintillator tile design. The fiber is imbedded in a groove in the scintillator tile.

5 Silicon Detectors

If cheap, radiation hard silicon could be developed, one could consider making a calorimeter using Silicon as the sampling medium. (See, for example, the work of the SICAPO collaboration.) The result would be a compact calorimeter which would be easy to segment, and which would have excellent position resolution. A calorimeter of this type is being considered for the far forward region of the H1 detector. A few planes of silicon in front of the calorimeter could be used as a pre-shower detector to assist in electron identification. Similarly, a few planes deeper within the module can be used for position resolution and shower profile measurement for electron identification.

Calibration of the energy deposit in silicon requires careful control of the uniformity of the thickness of the sampling layer and the active depth of the silicon. Uniformity has been demonstrated at the 1% level. Dead areas in such a calorimeter can be a problem. There will be inactive areas on a silicon plane between cells as well as at the corner of each cell where an electrode is attached for getting the

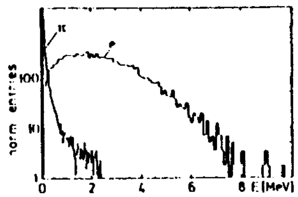

Figure 16: Deposited energy for 30 GeV electrons and pions in 400 μ m silicon behind 1.5 X_0 absorber.

signal out. Typical effective coverage is 96%.

Silicon detectors fabricated for a particle detection must have low leakage current (noise). An average current would be of order $13nA/cm^2$.

5.1 Preshower Detectors

Typically the calorimeter in a real detector will be preceded by somewhat less than a radiation length of material due to other parts of the detector, a magnet, and/or support structure for the calorimeter itself. Electrons incident on this material will begin to shower, and detection of greater than 1 $\sim$ mip of ionization in a "preshower" detector placed just in front of the main calorimeter can be a useful tool for electron identification. Figure 16 shows the signal obtained for 30 GeV electrons and pions in $400\mu m$ of silicon placed behind $1.5X_0$ of absorber material. In some cases, the resolution of the calorimeter can be improved slightly by detecting the preshowering condition.

5.2 Radiation Damage

The major effect of high dose radiation on Silicon detectors is to increase their leakage current and therefore degrade the noise performance of the calorimeter. The bulk current (which is $< 0.1nA/cm^3$) is increased 2 orders of magnitude by exposure to 100 Gy of protons and 3 orders of magnitude by 100 Gy of electrons. (Since Grays represent energy loss, and protons deposit more energy per particle in the Silicon, they are more damaging per particle.) 100 Gy of protons corresponds to about 3 10^{10} protons per square centimeter.

At the SSC, there are of order 10^{13}neutrons/cm^2 produced. The radiation dose in the forward region reaches 100 kGy or 10 Mrad per year. This radiation level is such that significant leakage current increase will occur within 10 days of operation. Recovery (annealing) of this damage is thus necessary for successful operation of such a device. Work is underway to study these phenomena. For example, one hour of heating at 200 degrees C can reduce the noise in an irradiated silicon detector by a factor of 3.5. Repeated cycles of radiation indicate that the damage is never completely annealed away. Calibration of such a detector will require careful study since it may vary depending on the time dependence of the radiation exposure.

6 LHC and SSC

Probably the most severe radiation environment for a calorimeter is the proposed Large Hadron Collider (LHC) at CERN. This machine has a planned luminosity of $10^{34}cm^{-2}s^{-1}$, and a time between bunches of 15 ns. Such a high luminosity requires radiation-hard, high speed devices. The dose rate is about 27 times higher than at the SSC. This factor is fairly easy to understand. It comes from the product of a luminosity ratio LHC:SSC of 40:1 and an inelastic proton cross-section (the primary beam loss mechanism) ratio of 86:100 due to the lower LHC energy.

The performance of a calorimeter at both the LHC and the SSC will depend to a greater extent than before on the constant term in the resolution due to the overall higher energy of the interesting physics processes at these machines. The constant term will depend on the effects of radiation damage as well as the response uniformity, shower containment, cell to cell variations, and module to module calibration differences. Both machines require large volume devices with fine segmentation since the higher energy requires both more depth (for good containment and somewhat finer segmentation (because the higher energy jets are more collimated). The approximate number of segments is

$$\phi\eta \text{ depth} \rightarrow (2\pi/0.1)(6/0.1)(2 \text{ or } 3)$$

which is about 10,000 segments.

Various calorimetry working groups have studied the design of SSC and LHC calorimeters. Some of the major issues include shaping times and pileup due to the short time between bunch crossings, linearity, calibration and other resolution requirements, segmentation, hermeticity for missing E_t measurements, electron identification using preshower detectors or transverse profile measurements near shower maximum, the effect of magnetic fields on the absolute calibration, radiation hardness and, of course, cost issues.

The types of calorimeters considered have included scintillator detectors using wave bars, tile fibers, or spaghetti designs, direct ionization devices using Liquid Argon or room temperature liquids such as TMS, TMP, or TMGe, silicon calorimeters, Liquid Xenon detectors for better electromagnetic resolution, and BGO or similar uniform or non-sampling detectors. Given that the QCD inclusive jet cross section is of order $300\mu b$ above 20 GeV, and that many interesting processes have cross sections of only a few pb, the calorimeter and the rest of the detector must be able to pick out interesting events at the level of a part in 10^8.

6.1 Physics Requirements

Before discussing in more detail some of the construction issues for these calorimeters, it is useful to consider the physics requirements, i.e., some of the processes of interest and their implications for the desired performance of the detector. Some of the things which we would like to be able to see, if they are there, are the Higgs, new Z's and W's, supersymmetric particles, leptons and inos, technicolor, lepto quarks, etc. In addition, there will be old physics, copious production of the W and Z, as well as the top quark if it is light enough, QCD jet and multijet final states, and multiple weak boson production.

Many of the signatures both of the new and the old physics involve lepton final states. This leads to the necessity of concentrating on electrons and electromagnetic calorimetry, muons—even using parts of the calorimeter as a muon identifier, and neutrinos using missing E_t in the overall detector design. One would probably include tau's in this list, except that their detection is very difficult and not very efficient. Detection of one prong tau decays is swamped by backgrounds from jets with one detected charged particle. Some success in tau detection can be achieved

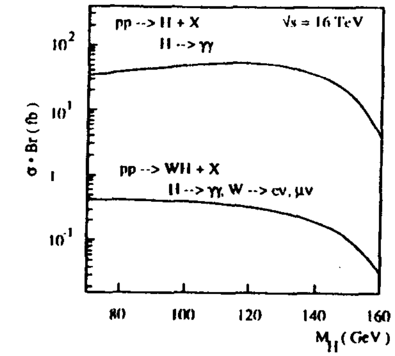

Figure 17: Cross section times branching ratio for Higgs production at the LHC.

by combining a 3 prong signature with the requirement that the invariant mass of the 3 prong be smaller than the τ mass. Even so, there is a large background from 3 prong jets. Along with the lepton final state, many interesting physics processes also produce several jets, and so, good jet energy resolution is also a desirable feature. Finally, the Higgs decay to two gammas provides a high resolution method of detecting this crucial component of the standard model, and this process as well as electron detection requirements argue for excellent electromagnetic resolution.

6.2 Higgs

Figure 17 shows the cross section times branching ratio in femtobarns (10^{-39}) for Higgs production at the LHC with subsequent decay into $\gamma\gamma$ and for W plus Higgs production with a $\gamma\gamma$ decay for the Higgs and electron or muon decay for the W. The low mass Higgs is narrow, so the $\gamma\gamma$ decay allows it to be separated with high resolution from the rest of the rather copious lowmass QCD background. The cross section of 10 fb gives a rate of 10^{-4}/sec or roughly a thousand events in a year's run. The trick here is to have good enough rejection of the QCD background to see the signal above the noise.

Since the final state has two bodies, an eta range of ± 2 is adequate. Figure 18 shows the p_t distribution for photons from a 100 GeV Higgs decay. The left plot is

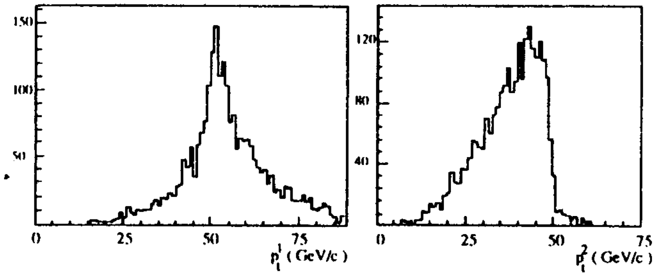

Figure 18: The p_t distribution for photons from a 100 GeV Higgs decay: The more energetic photon distribution (left) and the less energetic photon (right).

for the more energetic photon, while the right plot is for the lower energy photon. The overall acceptance is about 50% and can be increased by 45% by using ± 3 units of rapidity, however the signal significance increases only by 18%. This is because the heavy mass Higgs decays into $d\Omega$, most of which is covered in 2 units of rapidity, but the QCD background uniformly populates η. Thus the signal to noise decreases for larger η. This is a general feature of searches for heavy mass states.

Asymmetric cuts on the photons help eliminate background since requiring an imbalance in photon energy is equivalent to placing a p_t cut on the Higgs. Since the Higgs is massive, it has a more extended p_t distribution than the QCD background, so cutting at higher p_t improves the signal to noise.

Another channel where electromagnetic resolution in the calorimeter can be utilized to advantage is the four electron final state. The object is to detect a new state decaying to ZZ, in particular $H \rightarrow ZZ$. The interesting modes for detection are $eeee$ and $ee\nu\nu$. For heavier Higgs mass than is useful for the $\gamma\gamma$ state, the Z branching ratio becomes large, and again the excellent mass resolution achievable for electron pairs can be used to make the Higgs signal stand out above the QCD background. For the calorimeter, however, the four lepton final state requires a larger acceptance since the detection of all four leptons would give an efficiency going roughly like $\Delta\Omega^4$ except for some correlations between lepton directions. The spectrum of leptons is such that detection must extend down to 10 GeV for

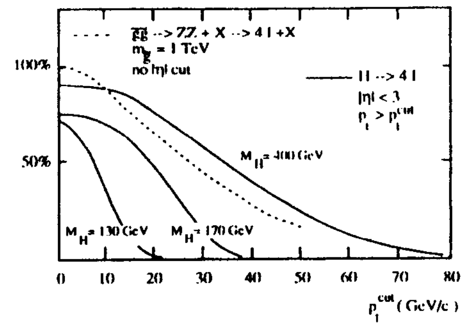

Figure 19: Detection efficiency for the ZZ mode as a function of the electron cut-off.

good efficiency. (See Figure 19.)

For the $ee\nu\nu$ case, a Z decaying into two neutrinos will result in a large missing E_t for the event. This is a more difficult signature than the four electron mode since the ability to detect this process above the QCD four jet background and, worse yet, the QCD two jet plus mis-measured missing E_t will depend on the missing E_t resolution which in turn depends on the hadronic resolution and the forward coverage. This will require larger rapidity coverage in the forward region to keep forward jets from contributing significantly to the missing E_t resolution. It is perhaps possible to use the forward calorimeter as a veto in the sense that if energy above some cut is detected there, the event is not considered in the $ee\nu\nu$ sample since any jet in that region significantly degrades the missing E_t resolution.

6.3 Pileup

At a luminosity of

$$L = 2\ 10^{34} cm^{-2} s^{-1}$$

there are approximately 26 inelastic events per bunch crossing at the LHC. The inelastic cross section is 86 mb so

$$(86\ 10^{-27})(2\ 10^{34})(15ns) = 26\ .$$

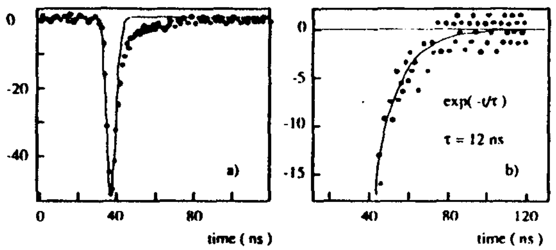

Figure 20: Time development of a hadron shower pulse (SPACAL).

The calorimeter cannot resolve this because there is a fundamental limitation in the time performance of a hadron calorimeter due to the shower formation time in the calorimeter. The SPACAL collaboration has measured (see Figure 20) that the hadron shower requires of order 45 ns to form primarily due to the slow neutron content. The neutrons in the shower are moderated (or slowed down) by collisions with a time constant of approximately 10 ns.

6.3.1 Minimum Bias Fizz

Since the events within one crossing cannot be resolved, these overlapped events will contribute a general noise level in the detector. Fortunately, while the track content of the events is large, the energy content is not. The events result from the very high (86mb) inelastic cross-section, but do not in general contain a great deal of high p_t activity. The events from the inelastic cross section are referred to as "Minimum Bias" events referring to the fact that to get them you need a trigger condition with minimum bias. In practice, this usually means triggering on a small amount of energy in some set of far forward counters. The overlapped events from this source will thus contribute a "fizz" or low level of activity everywhere in the detector (uniform in η). Fluctuations in this fizz will contribute to the resolution of any calorimeter. This pileup contribution will be proportional to the gate time for the calorimeter and also the area of integration in the calorimeter for a given physics process (usually referred to as a cone size and defined later). For a cone size

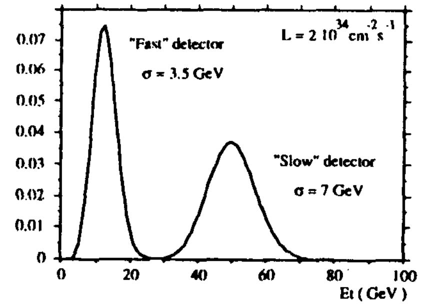

Figure 21: Distribution of minimum bias energy depositions for a slow and fast detector.

of 0.4, the LHC luminosity gives an equivalent rms contribution in the calorimeter of 6.2 GeV. For a 100 GeV jet, this would be equivalent to a contribution to the energy resolution of $60\%/\sqrt{E}$ and thus pileup would dominate the resolution for a calorimeter with intrinsic resolution of say $35\%/\sqrt{E}$. Figure 21 shows the difference between a fast and slow calorimeter indicating that this contribution can be reduced if the integration time of the calorimeter can be reduced (until 15 ns where one includes only one bunch). It is important to note here that this effect is 26 times smaller at the SSC which has roughly the same bunch spacing, a slightly higher inelastic cross section, but a reduced luminosity. To make full use of very high luminosity may require either fast calorimeters, or physics signatures which are not overly sensitive to resolution.

6.4 Cone Angles

When energy in the calorimeter is clustered or accumulated into jets, it is often done by collecting all of the energy contained in a cone centered on the largest energy deposit. The cone has a size in the $\eta\phi$ plane which is given by

$$\Delta R = \sqrt{\Delta\eta^2 + \Delta\phi^2}\ .$$

Typical cone sizes range from 0.7 to 1.0. If the cone is too large, the pileup contribution to the resolution will be large. If it is too small, losses from the cone will dominate the resolution. The optimum choice will depend both on the physics process of interest and the energy scale of the jets of interest. For example, high p_t W production makes pairs of jets with a small relative opening angle at the SSC. The use of a cut on the W p_t can enhance signals for final states involving t quarks since using higher p_t jets increases the average jet energy thus improving the jet energy resolution. A small cone size is in fact necessary to keep from merging jets in a single cone. At the same time, the high energy scale of the jets makes them less susceptible to losses out of the cone.

6.4.1 Shower-Track Matching

Another technique where pile-up has a crucial impact on the calorimeter performance is in the comparison of the position of a track with its (typically electromagnetic) energy deposition. This is often used for electrons to distinguish between real electrons and the overlap of a high p_t track and a compact energy deposition (usually an energetic π^0). Pileup can significantly reduce the efficiency of this cut. While it is certainly true that the increase in the track density reduces the efficiency for track finding, the main effect is that the random deposition of energy from the minimum bias events reduces the accuracy with which preshower and shower maximum detectors can determine both the position and the shape of the shower. Figure 22 shows the percentage efficiency loss as a function of the matching required between the track and the shower for the LHC using a "slow" calorimeter (with 60 ns integration time—it's actually moderately fast) and 20 GeV electrons. Again, a small cell size reduces the total contribution of the inelastic events. Reasonable efficiency for a slow calorimeter would require a cut as large as 1.6 cm which is about 4 times larger than similar cuts used at the Tevatron (CDF).

Due to the smaller physical size of electron and photon showers compared to hadron showers, the total pileup contribution is smaller. In this case, the inelastic events still affect the minimum usable EM energy deposition per calorimeter cell. The minimum bias contribution is typically a few hundred MeV per 0.1×0.1 in $\eta\phi$ per 10^{34} luminosity, and grows like $\sqrt{N}$. This raises an important point for

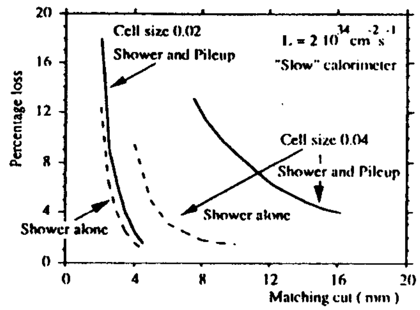

Figure 22: Losses in electron efficiency due to the effect of minimum bias deposits on shower matching cuts.

calorimeter design which limits the minimum distance of the calorimeter from the beams. Since the smallest reasonable cell for pileup integration is the electromagnetic shower size, the calorimeter must be kept a minimum distance from the beam to keep this size (which is measured in a fixed number of centimeters) from representing a large acceptance in $\Delta\eta\ \Delta\phi$ since the minimum bias background is constant per unit rapidity and phi. Thus, by moving the calorimeter back, the solid angle represented by the physical size of the EM shower will be smaller in $\Delta\eta\ \Delta\phi$ units and thus receive less background.

6.4.2 The Effect of Pileup on Electron Isolation

Often in searching for heavy objects like the top quark (and to some extent also bottom mesons), one takes advantage of the fact that transverse to the direction of the heavy object of mass m, the decay can generate a p_t of m/2. For semileptonic decays, this results in an increase in the average p_t of the decay leptons relative to the remaining jet activity for heavy objects. By requiring lepton candidates to be unaccompanied by other activity (isolated), one tends to select against events coming from light quark backgrounds. The isolation requirement also helps to make the electron easier to identify and improves the accuracy of the energy measurement. In the CDF detector, for example, one can cut on an activity in the hadron and electromagnetic calorimeter cells surrounding the electron at the

1 GeV level. As pileup increases, the natural level of background in such cells will increase and at the same point this cut will become ineffective.

6.5 Resolution

The decay of the Higgs to $\gamma\gamma$ is probably the best detection channel for the Higgs provided its mass is in the 80 - 130 GeV range. This channel also has the most severe resolution requirements. The signal to noise will improve with better electromagnetic resolution, so this should be optimized. Non-sampling calorimeters have better resolution than sampling calorimeters, but several other features of the calorimeter are also important. For example, the constant term in the resolution must be kept small. A good resolution calorimeter ($5\%/\sqrt{E}$) should have a constant term below 0.5%. Unfortunately, BGO which has very good resolution, is also subject to radiation damage. The calibration needs to remain accurate to limit the effective constant term from this source. NaI is too slow a calorimeter and would have a constant term dominated by pileup fluctuations. The calorimeter will also need good position resolution. The required mass resolution for a Higgs search translates to an angular precision requirement of 5 mrad for the calorimeter. Finally, the detector as a whole must be able to eliminate the hard pizero component of jet production. Note from Figure 23 that the fake gamma inclusive cross section is measured in hundreds of nanobarns at 20 GeV p_t, the inclusive real gamma rate is a few nanobarns and the desired Higgs rate is measured in femtobarns.

6.5.1 Pileup and Jet Resolution

Figure 24 illustrates the effect of pileup contributions on the ability to reconstruct jet pair masses. The top plot in Figure 24 shows the intrinsic resolution for two jets in a $pp \to ZH \to ee + bb$ event for a 100 GeV Higgs (without energy resolution or pileup contributions). The lower plots show the reconstruction of Z's with and without pileup in inclusive Z production. The pileup contribution has two effects. First, the additional 5 - 7 GeV rms in the cone will degrade the overall resolution, and, second, if a correction is not applied to the jet energy scale, the mass

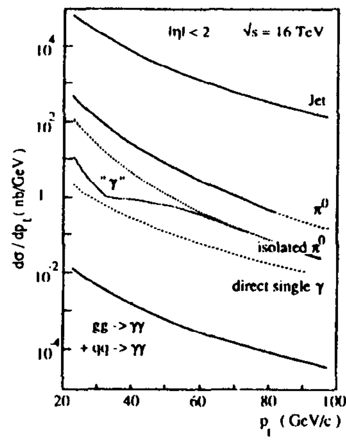

Figure 23: Photon sources at the LHC as backgrounds for Higgs searches.

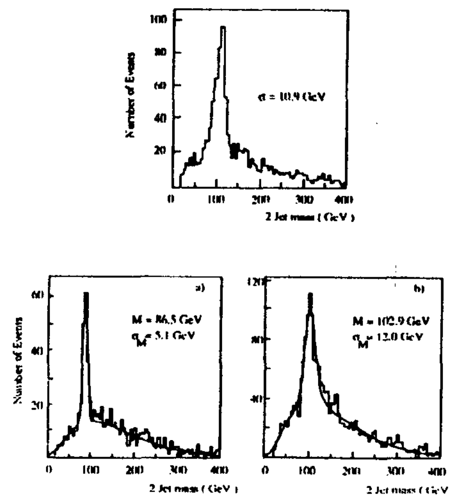

Figure 24: The effect of pileup on the 2 jet mass resolution: (top plot) two jets reconstructed in $pp \to ee + bb$ (bottom plot) two jets from $Z \to jj$ without pileup (left) and with 40 minimum bias events (right). Smearing due to finite calorimeter resolution is not included.

calibration will shift upward by about twice the mean pileup.

6.6 Acceptance

Different physics processes can make quite different demands on the acceptance requirements of the calorimeter. The central region of the calorimeter (to η of about 2, $\theta > 15$ degrees) is important for inclusive electrons, electron pairs, W and Z production, inclusive Z with decay to electron and muon pairs for searches for associated production with the Higgs, and for studies of heavy particle production like the top. This is because a few units of rapidity covers a large fraction of the total solid angle, and while QCD production populates η in a uniform manner, heavy particle decay populates Ω.

The endcap region $15 < \theta < 5$ is necessary for increasing the total efficiency for multibody final states, for example, four electron final states which are interesting due to the possibility of observing Higgs decays to two Z's. This kind of state requires a large total $\Delta\Omega$ for good efficiency. At very small angles (the plug region), it is necessary to have calorimetry for use in calculating the missing transverse energy, which is important for processes with neutrinos. Top quark production with semileptonic decay of one of the tops will produce missing E_t which is often used as an analysis cut. For the SSC or LHC, Higgs decay to two Z's can be detected by tagging the decay of a Z to two neutrinos using missing E_t and detecting the second Z with lepton pairs. This mode (due to the 3 families and the higher ν branching ratio) is more efficient by a factor of 6 than the 4 electron mode.

7 New Designs

Over the past three years, there have been many research and development projects for calorimeter design and these have yielded several new and interesting techniques for calorimeter construction. The "Accordion" design shown in Figure 25 is one example. In this type of calorimeter, the absorber material would be shaped like an accordion rather than being made of plates which are traditionally arranged perpendicular to the incident particle direction. Shower formation is unaffected

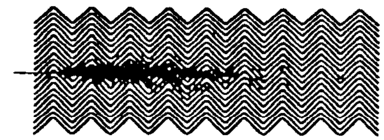

Figure 25: An Accordion design for absorber material can facilitate bringing signals to the rear of the detector.

except that for the same sampling thickness the plates need to be thinner by $\cos\theta$. The advantage of this type of construction is that in a large calorimeter, the signals (either wires for ionization calorimetry or wave bars or fiber bundles) need to make their way to the rear of the module where there is room to put electronics and/or phototubes. In ionization calorimeters, bringing the signals to the rear of the device is usually done by having holes in the plates through which wires, electrodes or cables pass. For scintillator devices, the wavebars or fibers travel up the edge of the device. Either of these solutions produces dead regions in the calorimeter and additional mechanical and construction difficulties. Figure 26 shows another solution to this problem which has been investigated by the SPACAL collaboration. For this calorimeter, fibers run along the length of the module from front to back. The primary difficulty in this case is how to achieve longitudinal segmentation. Suggestions have included making wedge shaped modules where the fibers which terminate at different depths are grouped together, having fibers throughout the module which are different lengths, and color coding the information from different depths using different color fluors and filters as shown in Figure 27.

8 Calorimeter Depth

The choice of thickness for the hadron calorimeter can be quite important both for the performance of the device, and also for its overall cost. If the calorimeter is too thin, fluctuations in the energy exiting the rear of the calorimeter will affect the resolution and linearity. On the other hand, the rear of the calorimeter may collect only a small percentage of the total energy, but since it is situated at the

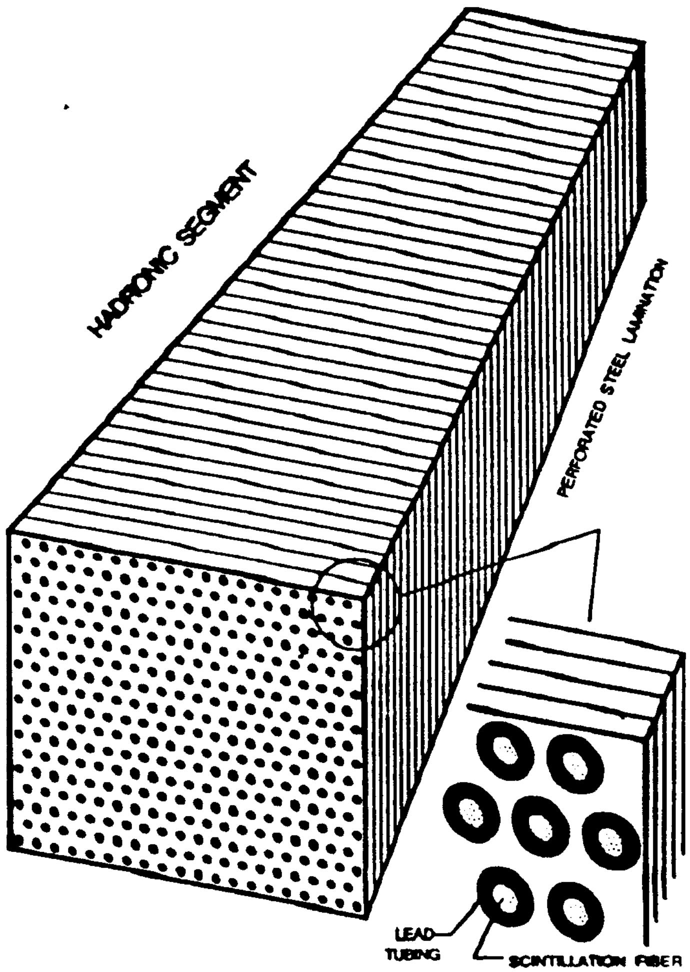

Figure 26: SPACAL calorimeter with longitudinal fibers.

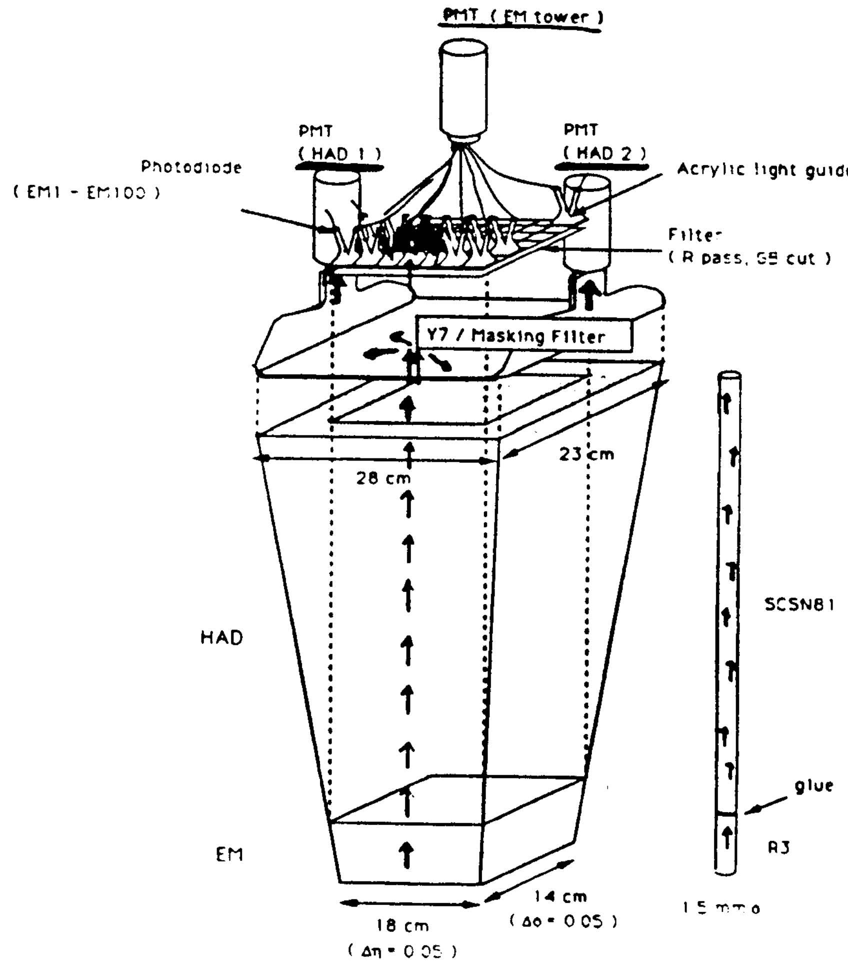

Figure 27: Color coding of depth information in a fiber calorimeter.

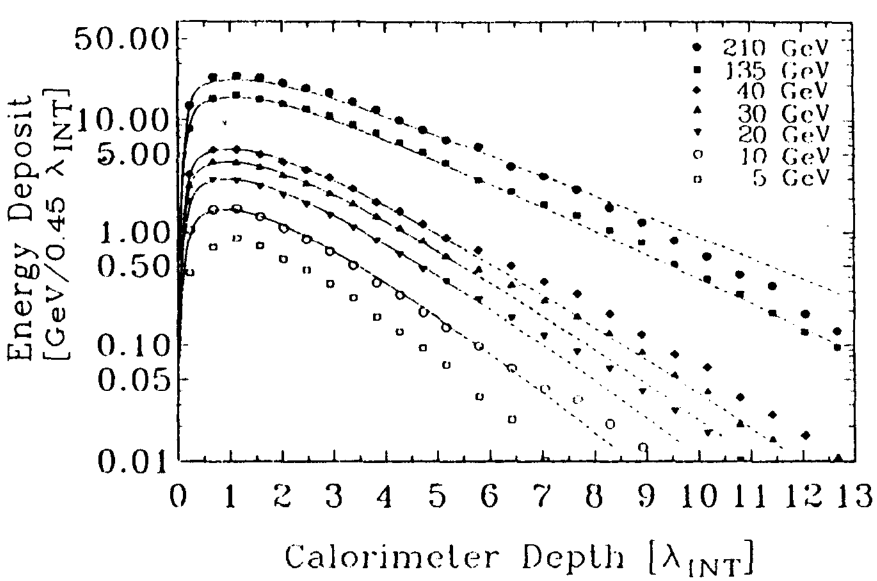

Figure 28: The longitudinal shower profile measured by WA78.

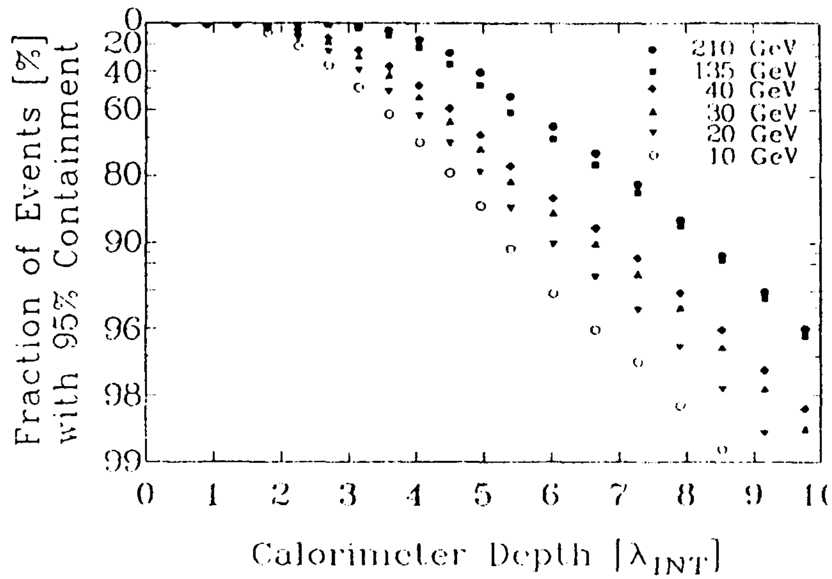

Figure 29: Fraction of Events with 95% containment as a function of calorimeter depth.

largest radius away from the center of the detector, it can represent significant volumes of materials, and thus high cost. It is useful to examine whether the small percentage of energy is being measured in a cost effective manner.

The data shown in Figure 28 are taken from measurements of the longitudinal shower profile by WA78 at CERN [3]. The WA78 hadron calorimeter had a 5.4 λ section constructed from 12 modules of depleted Uranium. Each module consisted of 4 alternating sets of 10 mm U and 5 mm scintillator. This was followed by an additional 8 λ calorimeter constructed from 13 modules of Iron where each module contained 4 sets of 25 mm Iron and 5 mm scintillator. A fit to the measured shower development curve (good above 10 GeV) is given by

$$\frac{I}{I_0} = \frac{1}{1+kx}\frac{dE}{dx} = E_0\left\{\alpha\frac{b^{a+1}}{\Gamma(a+1)}x^a exp(-bx) + (1-\alpha)\, c\; exp(-cx)\right\}$$

$$\begin{gathered} a = 3 \\ b = 19.5 \\ \alpha = 0.13 \pm 0.02 \\ c = (0.67 \pm 0.03) - (0.166 \pm 0.003)\ell n\left(\frac{E_0[GeV]}{50}\right). \end{gathered}$$

Figure 28 gives information about the average energy deposition at each depth, but does not indicate the fluctuations in this energy which are in turn responsible for determining what fraction of the events will be well contained within a calorimeter of a certain depth. This information is shown in Figure 29. For example, at 210 GeV, 96% of the events have at least 95% of their energy contained in a calorimeter of depth 10 λ.

The depth criterion used by the ZEUS collaboration in specifying their calorimeter was that they wanted at least 95% containment of 90% of the jets at the machine's maximum kinetic energy. The remainder of the energy was to be col-

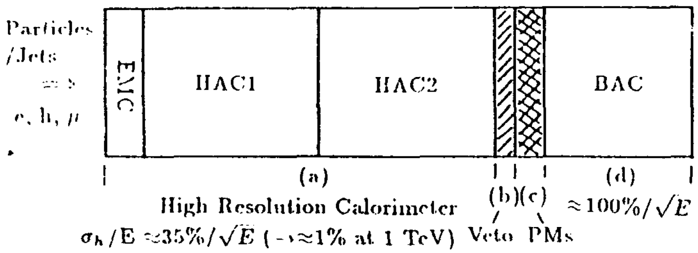

Figure 30: The four main sections of the ZEUS calorimeter.

lected in a moderate resolution (and cheaper) "backing" calorimeter. Thus the full calorimeter consists of four parts as shown in Figure 30; an electromagnetic section, two hadronic sections with $35\%/\sqrt{E}$ resolution and the backing section with $100\%/\sqrt{E}$ resolution. Figure 31 gives the required calorimeter depth for containment of 90% of single hadrons for containment fractions between 90% and 97.5%. By comparing this to Figure 32 which shows the same information for jets, one can see that it is, as expected, easier to contain jets than single hadrons. The difference at 200 GeV is about 1.5 λ. Actually the " jets" in these plots are single hadrons in the test beam which have been selected in the analysis because the shower initiated in the first 1.1 λ of the module.

While direct information at 1 TeV is not available, the WA78 fits can be extrapolated to 1 TeV to obtain the plots shown in Figures 33 and 34 for single hadrons and jets. Thus the ZEUS requirement of 95% containment of 90% of the jets would lead to a calorimeter thickness of 8.5 λ at 1 TeV.

9 Material in Front of the Calorimeter

Real calorimeters often have a number of structures in front of them such as beam tubes, vertex detectors, tracking detectors, magnetic coils, coil services, coil and/or calorimeter cryostats, calorimeter support structures, and cables and electronics for other parts of the detector. In the ZEUS detector this material thickness ranges from 1 to 1.5 radiation lengths but there are smaller regions

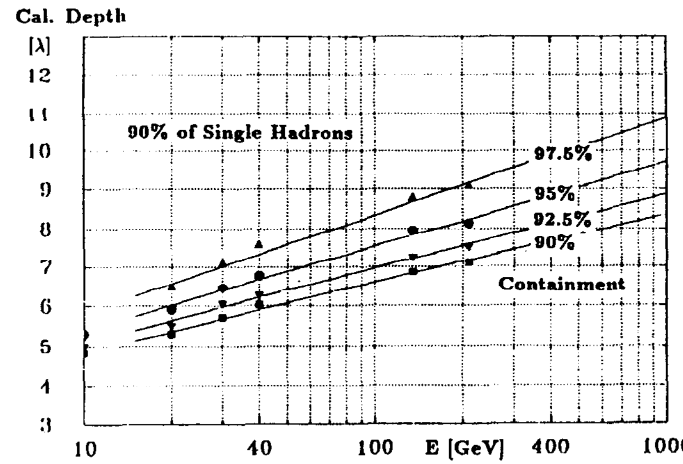

Figure 31: Calorimeter Depth required for Different Fractions of Shower Containment for 90% of Single Hadrons as a Function of the Energy.

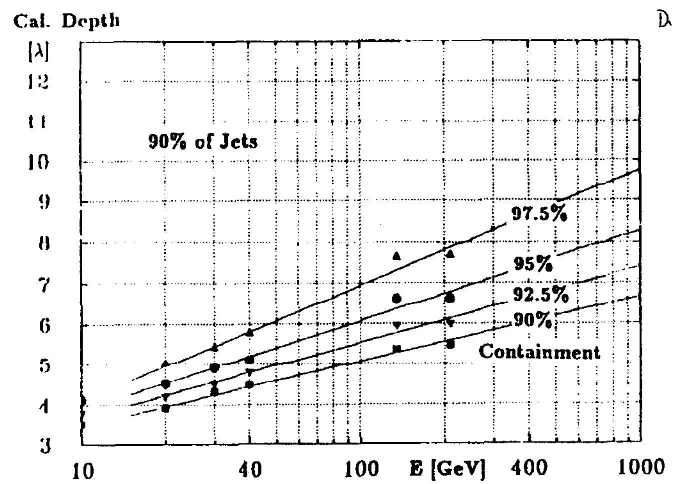

Figure 32: Calorimeter Depth required for Different Fractions of Shower Containment for 90% of 'Jets' as Function of the Energy.

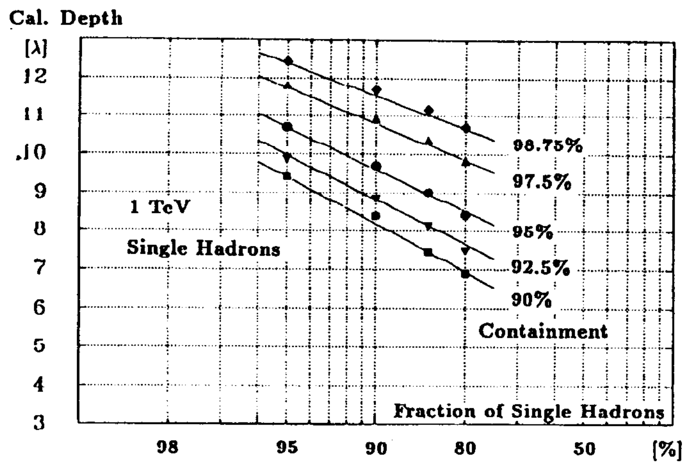

Figure 33: Extrapolated Calorimeter Depth requirement for Different Fractions of Shower Containment for 1 TeV Single Hadrons as Function of the Fraction of Single Hadrons which are contained.

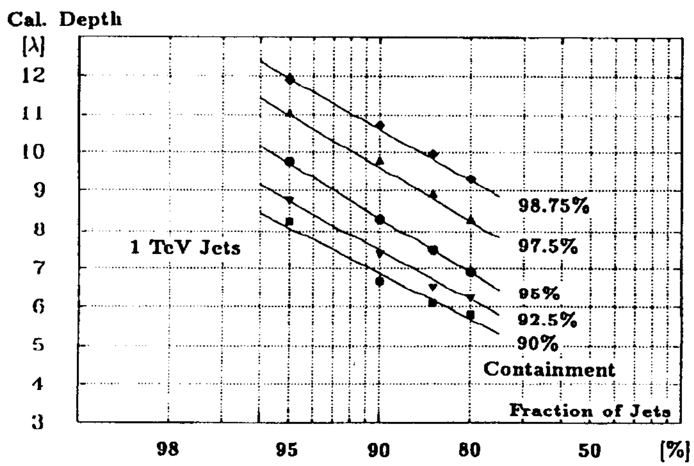

Figure 34: Calorimeter Depth required for Different Fractions of Shower Containment for 1 TeV 'Jets' (Extrapolation) as Function of the Fraction of 'Jets' which are so contained.

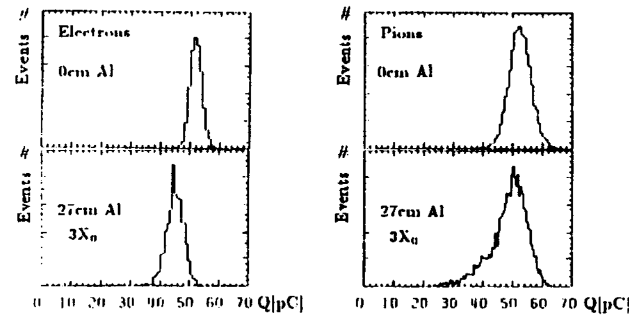

Figure 35: The energy spectra for 30 GeV electrons and pions with and without 27 cm AL in front of the calorimeter.

with as much as 4 radiation lengths due to mechanical support structures. The material causes both a downward shift in the calibration and an increase in fluctuations (degradation in resolution) due to variations in the amount of energy lost in the material. Electron energy distributions in an electromagnetic calorimeter following material remain gaussian, but pion energy distributions become strongly asymmetric due to the occasional production and subsequent showering of π^0's. Figure 35 shows the energy spectra for 30 GeV electrons and pions with and without 27 cm of Aluminum in front of the calorimeter and illustrates this behavior.

Sometimes the material in front of the calorimeter can be not only quite thick, but also complicated to describe. Figure 36 shows the region at the end of the superconducting coil in the CDF detector where the coil thickens, and there are axial support rods to hold the coil in position. This complex region is quite difficult to describe to the detector simulation program except on average. In practice, events with jets or particles traversing regions of this type often have to be discarded due to poor resolution. If one is not careful in the design of the overall detector, too many regions of this type may have a severe effect on the acceptance of the apparatus.

A study using the GEANT monte carlo for electron showers in Aluminum absorbers shows that this material can have a substantial effect on the calorimeter resolution. Figure 37 shows the mean energy loss as a function of energy, and

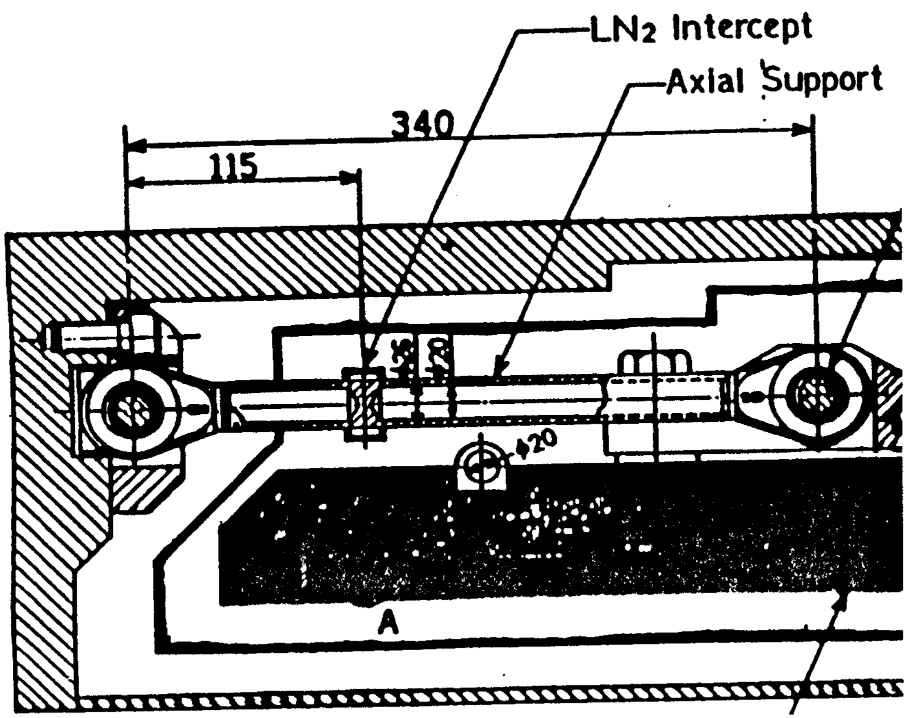

Figure 36: End region of the CDF coil structure.

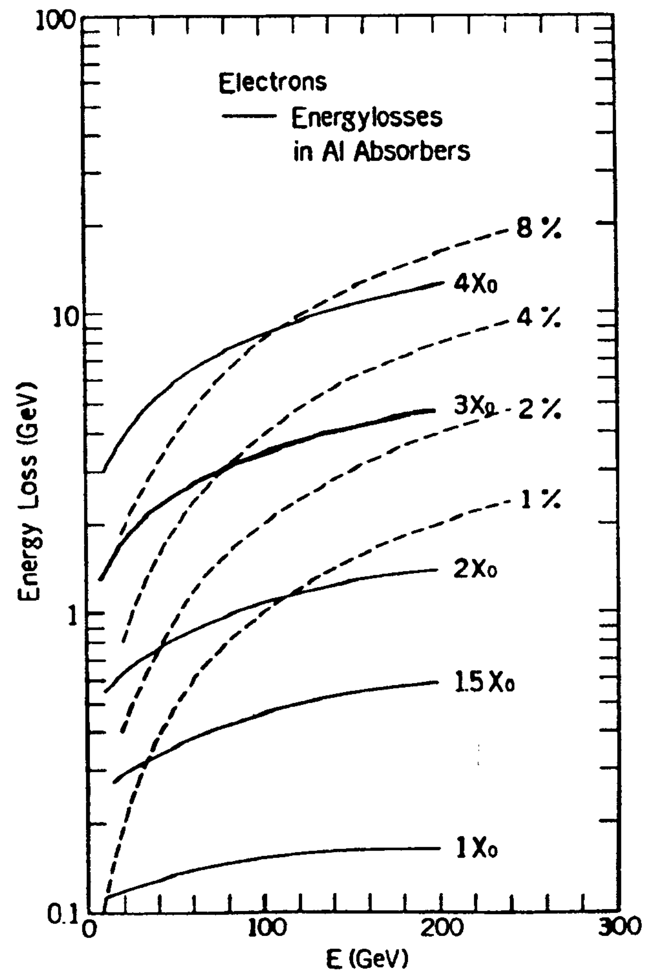

Figure 37: Mean energy loss as a function of energy for an Aluminum absorber.

Figure 38 shows the rms fluctuations in this energy loss. Also shown on the figure with dashed curves are lines which represent fixed percentages of the incident energy. Thus suppose one were attempting to build a calorimeter with very good resolution but with 2 radiation lengths of material preceding it. Note that the mean energy loss for 2 radiation lengths crosses the 1% curve at about 100 GeV. This means that there will be a greater than 1% shift in the calibration for all energies less than 100 GeV. If this shift is known to 25%, the calorimeter scale is unknown to 0.25% at 100 GeV, about 0.5% at 40 GeV and so on.

The fluctuations are even more important. For 2 radiation lengths, all energies less than about 30 GeV will have contributions to the resolution of order 1%, and 2% at 20 GeV. These fluctuations contribute to the constant term in the resolution $a/\sqrt{E}+b$ so that a calorimeter with $2\%/\sqrt{E}$ at 30 GeV would have a resolution dominated by these fluctuations.

A calorimeter region with 4 radiation lengths in front of it has a resolution contribution greater than 3% for energies all the way up to about 120 GeV! Another way of viewing this problem is shown in Figure 39 which gives the allowable absorber thickness versus the rms contribution to the resolution for various energy electrons. If the contributions are to be less than 2.5% for all energies above 10 GeV, the material thickness (Aluminum) must be kept less than 2 radiation lengths.

10 The Electromagnetic Shower

The size of an electromagnetic shower scales with radiation lengths (X_0) in the longitudinal direction. For Iron, Lead and Uranium, this quantity is 1.76 cm, 0.56 cm and 0.32 cm, respectively. In the transverse dimension, it scales with the Moliere radius

$$r_m = \frac{21(MeV)}{\varepsilon} X_0$$

where the constant 21 comes from

$$\sqrt{\frac{4\pi}{\alpha}} m_e c^2 = 21.2 MeV \quad .$$

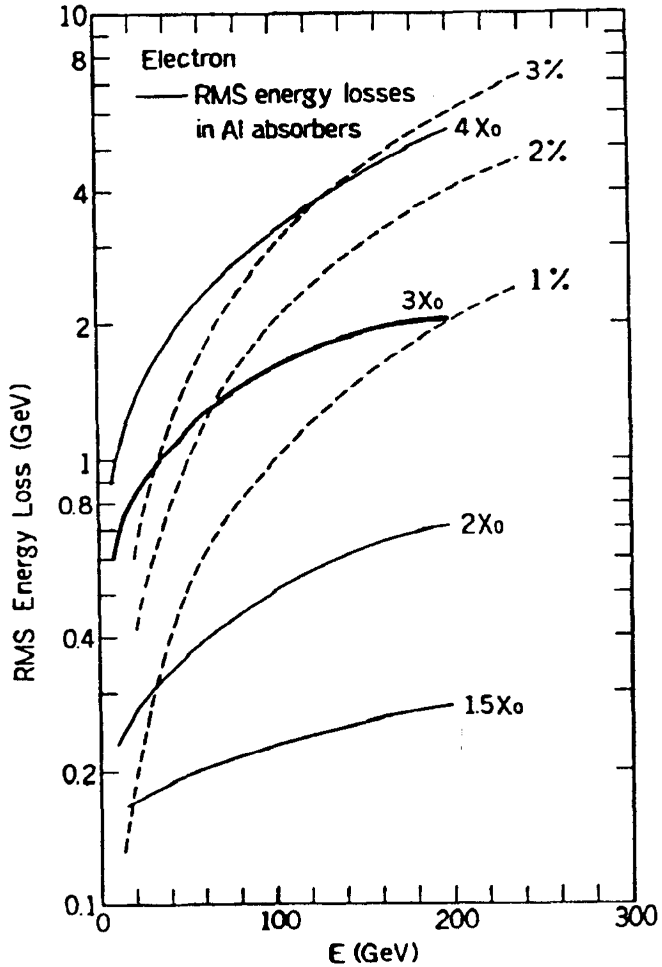

Figure 38: RMS fluctuations in the energy loss for an Aluminum absorber.

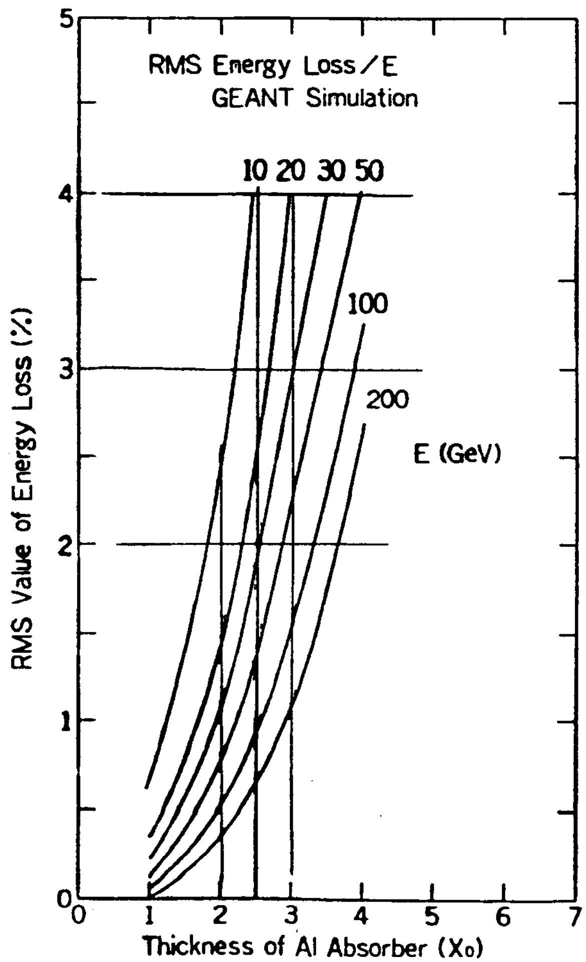

Figure 39: The allowable absorber thickness as a function of the rms contribution to the resolution for electrons.

The Moliere radius gives an approximately material independent lateral scale. A cylinder of radius $2r_m$ contains 95% of the shower energy. As can be seen, the Moliere radius is defined in terms of a critical energy

$$\varepsilon = \frac{dE}{dx}_{min} X_0$$

which is the energy lost in a radiation length by a minimum ionizing particle. For electrons, (which are never minimum ionizing) a more useful empirical definition is

$$\varepsilon = \frac{800\text{MeV}}{Z + 1.2} .$$

The radiation length is given to good approximation by

$$X_0 = \frac{716.4 gcm^{-2} A}{Z(Z+1)\ell n\left(287/\sqrt{Z}\right)} .$$

The radiation length of composite materials is calculated from

$$\frac{1}{X_0} = \sum \frac{f_i}{X_{0i}} .$$

It is interesting to note that because the pair production cross section for photons is

$$\sigma(\text{pairproduction}) = \frac{7}{9}\frac{A}{X_0 N_A}$$

the smaller photon cross section leads to an increase in the amount of energy carried by photons toward the back of the shower.

From the formulae above, one can see that radiation lengths scale like A/Z(Z+1). Ionization loss scales with Z and A like Z/A since

$$-\frac{dE}{dx} = 4\pi N_A m_e c^2 z^2 \frac{Z}{A}\frac{1}{\beta^2}\left[\ell n\left(\frac{2m_e c^2\gamma^2\beta^2}{I}\right) - \beta^2 - \frac{\delta}{2}\right]$$

where I is the ionization constant approximated by 16 $Z^{0.9}$. Putting these two together, one can see that the critical energy will scale like

$$\epsilon \sim \frac{1}{Z+1} .$$

	BaF_2	BGO	$NaI(Tl)$	$C_sI(Tl)$
X_0 (cm)	2.1	1.1	2.6	1.85
$\frac{dE}{dx}$ (MeV/cm)	6.6	9.0	4.8	5.6
emission(nm)	220,310	480	410	565
decay (ns)	0.6,620	300	250	1000

Table 1: Properties of typical materials used in non sampling detectors.

10.1 Non-sampling Detectors

Electromagnetic shower detectors are conveniently divided into sampling detectors where the shower is produced in dense absorbers and sampled after each absorber, and non-sampling detectors where the sampling material is also the showering medium. Most of these detectors depend on the collection of light in the showering medium and are read out by phototubes, though there are some low energy examples of detectors where the energy readout depends on the direct collection of ionization losses. Examples of useful media include Barium Fluoride, BGO, NaI, Lead Glass, Cesium Iodide, and, at lower energies, (proton decay experiments, for example) water. In principle, any dense medium with good light transmission properties would be usable, but, in addition, one would like the material to produce light in an easily detectible band of wavelengths, and one would like the time constant of the produced light to be fast.

Table 1 shows some of the properties of typical materials used for non-sampling calorimeters. Barium Fluoride has both a fast and a slow component to the light output as do many other materials. The performance of the calorimeter will depend on which components of the light are used and on how the signals from the detectors are gated.

Since non-sampling detectors tend to have better intrinsic resolution, leakage effects can be very important, and can easily dominate the resolution if the calorimeter is too thin. As is the case with hadron calorimeters, partial restoration of the resolution can be achieved by measuring the leakage crudely with a low precision backing calorimeter. The leakage fluctuations are Poisson processes and tend to have equal mean and rms values. A BGO crystal which is 24 cm long will have a resolution (σ_E/E) of slightly less than 1% at 50 GeV, but a 20 cm long crystal would have a resolution more than three times worse.

10.2 Sampling Fluctuations

If the sampling medium cannot be made dense enough, a non sampling detector becomes physically very thick. To avoid this, the shower must be initiated and sustained in a different media. By alternating sampling layers with denser material, the shower development can be "sampled" even though some of the energy deposition will be hidden in the dense medium. The ratio of sampling layer to material thickness should be adjusted whenever possible to equalize the calorimetric yield for electromagnetic and hadronic interactions. For Iron, Lead, and Uranium, the material to sampling ratios required are approximately 10:1, 4:1, and 1:1.

The energy deposited in the sampling layers is due to particles which shower in the dense medium and then cross the sampling layer. If we assume for simplicity that all of these particles are minimum ionizing, and that the thickness of the layer is ΔX, then the total energy deposited will be

$$E_s = N\frac{dE}{dx_s}\Delta x$$

where N is the total number of such particles.

The value of N can be calculated by using the critical energy ϵ which is the minimum ionization energy lost in a distance of one radiation length. Thus E/ϵ will be the total path length in the shower measured in radiation lengths, and

$$L = \frac{E}{\epsilon}X_0$$

will give the total path length in the shower. The number of tracks crossing the sampling layers for a shower which is completely absorbed in a calorimeter of thickness T will be

$$N = \frac{E}{\epsilon}\frac{X_0}{T} .$$

Each particle gives a signal E_s so the total signal output is NE_s and the fluctuations are

$$\sigma = E_s\sqrt{N} .$$

The resolution of the calorimeter will be given by

$$\frac{\sigma}{E} = \frac{1}{\sqrt{N}} = \sqrt{\frac{\epsilon T}{E X_0}} \ .$$

Actually this simple model gives an optimistic estimate of the error primarily because of the correlations in signal between adjacent gaps which occur if the sampling is fine enough so that particles cross more than one sampling gap. A correlation of 100% between two gaps increases the error by $\sqrt{2}$ and three gaps by $\sqrt{3}$. The correction for these correlations will depend on the thickness of the dense medium. The thicker the material, the smaller the correlation will be between adjacent samples. We have also assumed that all tracks are minimum ionizing and that tracks cross the gap perpendicular to the sampling layer direction. Non-normal incidence of some of the tracks requires that the thickness T be replaced by $T/\cos\theta$ where θ is a small effective angle averaged over the tracks.

10.2.1 Iron and Lead

Using the simple model of the previous section, and the critical energies of Fe and Pb which are 20.5 MeV and 7.2 MeV, respectively, the ratio of the resolution for these substances will be

$$\frac{\sigma_{Fe}}{\sigma_{Pb}} = \sqrt{\frac{\varepsilon_{Fe}}{\varepsilon_{Pb}}} \approx 1.7 \ .$$

To achieve the same resolution in iron, we would need to decrease the sampling thickness by a factor of 3. Since Iron and Lead have radiation lengths which differ by about a factor of 3, (1.76 cm for Fe and 0.56 cm for Pb), it would require the same physical thickness in centimeters for the dense media. Unfortunately, this is inconsistent with the ratios required for balancing the yields from electromagnetic and hadronic interactions.

10.3 Projective Geometry

The calorimeter can be constructed out of segments which all point like wedges of a pie toward the origin of the particles to be measured. In this case, we say that the geometry of the calorimeter is projective. The major advantage of this approach is that it minimizes the number of physical segments of the calorimeter across which shower development occurs. The principal disadvantage is that it can greatly complicate the mechanical construction of the device. In non-projective geometries, the depth of the calorimeter varies with incident particle position, and any dead regions in the device due to structural supports can have very large effective thickness for particles which cross them at small angles. In addition, showers can share across multiple segments which means that sharing between nearby energy depositions can be more difficult to disentangle.

Projective towers are not all the same physical size, nor are they usually of uniform shape. This requires a large number of dissimilar pieces to be constructed to assemble a module and can therefore increase construction costs. In the calibration of the detector, differences in the shape and size of various modules can make calibration more difficult when compared to calibrating a large number of identical units, but the physical response to towers or calorimeter segments arranged in a projective manner can be easier to understand given a smaller spread in incident particle angles and shower patterns. In general, it is easier to design devices which are cylindrical and projective in the azimuthal angle ϕ but not in θ or η, the Crystal Ball detector being a notable exception.

10.4 Electromagnetic Position Resolution

I would like to illustrate how to optimize the position resolution from a non-sampling electromagnetic detector using the GAMS spectrometer [4]. The detector was a lead glass calorimeter constructed from 32 x 32 mm blocks which gave a position resolution of 3 mm. Note that the expected resolution from cells of size 32 mm would be $32/\sqrt{12} = 9.2$ mm, so this represents a factor of 3 improvement. The usual way of calculating the position of a shower which is spread over several cells is to calculate the energy weighted centroid of the shower. This energy weighted mean, however, leads to a strong bias in the position estimates toward the center of the cells. The mean would, in fact, be a good estimator of the position if the transverse shower shape were uniform with distance from the shower core, but it's not.

In fact, the transverse distribution of shower energy is approximately exponential (good to about 10%). The transverse shape can be represented even better by two exponentials

$$a_1 \exp(-x/b_1) + a_2 \exp(-x/b_2).$$

In the case of the GAMS spectrometer, $b_1 = 4.5\mathrm{mm}, b_2 = 12\mathrm{mm}$, and $a_1/a_1 = 0.14$. The energy weighted mean is given by

$$X_0 = 2\Delta\frac{\sum iA_i}{\sum A_i}$$

where the A_i are the amplitudes in the ith cell and Δ is the half width of a cell. If the shower shape is a single exponential, it is not difficult to show that the true center and the estimate X_0 are related by

$$X_c = b\ \sinh^{-1}\left(\frac{X_0}{\Delta}\sinh(\delta)\right)$$

where $\delta = \Delta/b$. This formula can be used as a correction, or a better estimate (X_b) can be formed from the ratio of the largest energy cell and its neighbors.

$$X_b = \Delta - b\ \ln\frac{1}{2}\left(\frac{A_i}{A_{i+1}} + 1\right)$$

This ratio shows the same two exponential form as the transverse shower shape (see Figure 40).

Figure 41 shows a direct comparison of the true position, and the value calculated from the energy weighted mean and shows how the simple position estimates tend to be biased toward the cell centers.

In an actual experiment, there are a number of additional factors which need to be considered in the calculation of position. First, we would like to have a two dimensional equivalent of the previous results, second, the parameters of the transverse shower shapes must be determined, and, finally, angular and energy dependent effects must be taken into account.

The CCOR experiment used two arrays of lead glass blocks for an electromagnetic detector. Test beam data from a 3 x 3 array of blocks were used to find the ratio of adjacent block pulse heights as the beam was scanned across the front of the blocks (see Figure 42). This data determines the shape of the transverse shower curve which is then fit. Figure 43 shows similar data taken when the inci-

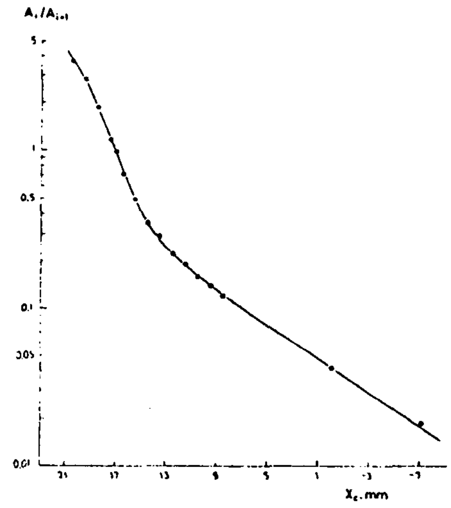

Figure 40: The ratio of the nearest neighbor cell to the largest cell as a function of shower coordinate.

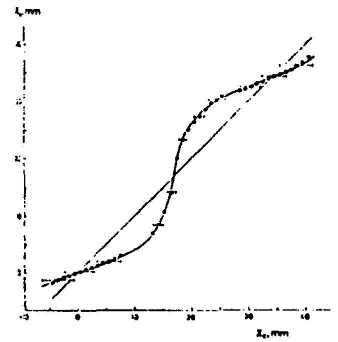

Figure 41: Comparison of the true and calculated (using energy weighted means) positions when the energy weighted mean is used to estimate position.

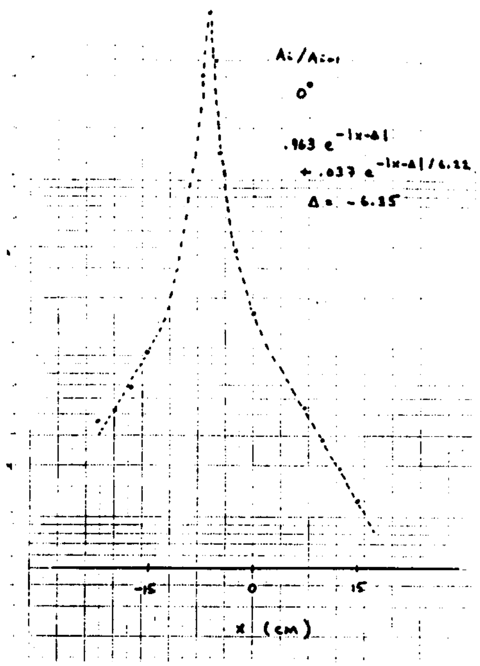

Figure 42: The ratio of adjacent block pulse heights as a function of beam position. (CCOR)

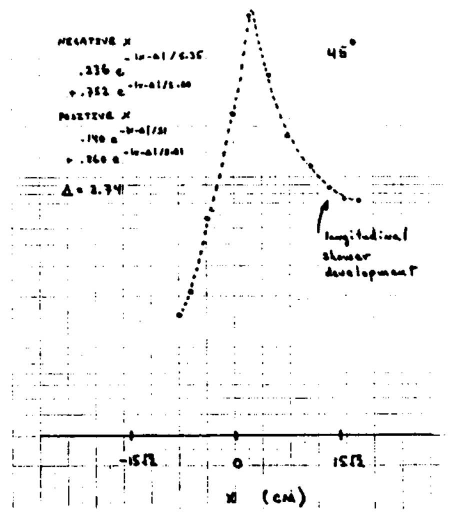

Figure 43: The ratio of adjacent block pulse heights at 45 degrees.

dent beam is at 45 degrees relative to the front face of the calorimeter. The beam points into the blocks on the right side thus increasing the pulse height there. The position of the point where the adjacent pulse height ratio is 1, gives the incident position of the beam for the normal incidence case, but this is no longer true for non-normal incidence. In this latter case, the shower center is found at an effective depth inside the calorimeter, and a correction which depends on the longitudinal shower development must be applied to find the incident point at the front face. Figure 44 shows a comparison of the resolution with and without these corrections for these two angles. For normal incidence, the position resolution is 2.7 cm without, and 0.47 cm with the correction, an improvement of more than a factor of 5. At 45 degrees, the resolutions are 1.0 cm and 0.47 cm, respectively. Actually, the angular dependence of signals from lead glass is complicated by the fact that they are produced by Cerenkov radiation which has a complex reflection pattern off the sides of the glass blocks. This dependence on Cerenkov radiation for signal output becomes an advantage however when doing a Monte Carlo sim-

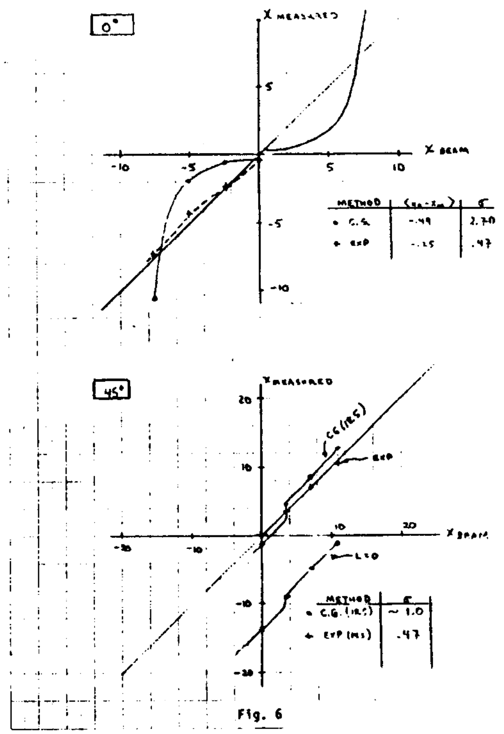

Figure 44: Comparison of the resolution before and after corrections for zero and 45 degrees.

ulation of the shower behavior, because it provides a natural threshold ($v = c/n$) below which particles do not produce light, and therefore the shower does not need to be simulated for such soft particles.

10.5 Longitudinal Shower Shapes

The longitudinal shower distribution is well described by an incomplete Gamma function (related to a partial integral of the gamma function)

$$\mathrm{P(a,x)} = \frac{1}{\Gamma(\mathrm{a})}\int_0^{\mathrm{x}} \mathrm{e^{-t}t^{a-1}dt}$$

where the gamma function itself is defined as

$$\Gamma(\mathrm{z}) = \int_0^{\infty} \mathrm{t^{z-1}e^{-t}dt}$$

and for integers, $\Gamma(n+1) = n!$. The shower energy deposited in a thickness t is

$$\frac{\mathrm{dE}}{\mathrm{dt}} = E_0 b \frac{(bt)^{a-1}e^{-bt}}{\Gamma(a)} \quad .$$

[5] The constants a and b in this parameterization vary slowly with energy and material type. The physical reason for this relationship is that the shower deposition is due to the sum of a large number of Poisson processes. The probability distribution is also related to the chi-squared distribution for n degrees of freedom

$$\mathrm{f(z,n)} = \frac{1}{2^{n/2}\Gamma(n/2)}\mathrm{z}^{n/2-1}\mathrm{e}^{-z/2}$$

with integral distribution

$$\mathrm{P}(\chi^2|\nu) = \left[2^{\nu/2}\Gamma\left(\frac{\nu}{2}\right)\right]^{-1}\int_0^{\chi^2} (\mathrm{t})^{\frac{\nu}{2}-1}\mathrm{e}^{-\frac{t}{2}}\mathrm{dt} \quad .$$

Note the similarity between this chi-square distribution and the incomplete gamma function which approximates the longitudinal shower shape. There are lots of nice approximations for these functions (see, for example, Abramowitz and Stegun 26.4.2, 26.4.19) and therefore similar useful approximations for longitudinal shower shapes. For example, the asymptotic form for these functions (and thus the form of longitudinal leakage) is $e^{-\lambda t}$ (see table below). Further, the chi-square distribution which is related to the integral of the energy remaining after a fixed depth (the leakage) has mean n and variance 2n.

E (MeV)	E_0	a-1	b	λ
100	4.54	1.00	0.515	0.32
300	7.18	1.45	0.493	0.31
500	8.24	1.65	0.476	0.31
700	8.32	1.84	0.470	0.31
1000	8.58	2.03	0.468	0.30
5000	10.88	2.74	0.454	0.27

Table 2: Shower parameters from Longo and Sestilli for showers in lead glass.

Given the relationship between the chi-square and the energy distribution, it is possible to use confidence level tables such as are contained in the particle data group booklet, which are integrals of chi-square distributions, to estimate shower leakage. If one uses $Z = 2bt$ for the integral of a chi-square with $n = 2a$ degrees of freedom, where a and b are shower parameters, t represents a thickness in radiation lengths. For example, with a 10 GeV shower Table 2 gives $b \sim 0.5$, $a \sim 4.0$. Using $n = 2a = 8$ degrees of freedom, if you want to require 5% leakage, we find a 95% confidence level (5% loss) corresponds to a chi-square of $\chi^2 \sim 15$ which gives a required thickness t of $15 = 2bt$ or approximately 15 radiation lengths. These relationships are useful to know both for estimating shower behavior, and for parameterizations of showers in monte carlos.

For large thicknesses, we learn from this analysis that the longitudinal profile begins to fall exponentially, with a shape $\exp^{-\lambda t}$. Note from Table 2 that the value of λ approaches a value of about 0.3. The reason for this is that, at the back of the shower, there are mostly photons (due to the longer conversion length of photons than radiation length of electrons). The energy spectrum of the photons at the rear of the shower will be dominated by behavior of the photons with the minimum absorption. Figure 45 shows the energy behavior of the Compton and pair cross sections (measured in cm^2/g) as a function of energy. Notice that the minimum is in fact 0.30.

The depth at which the maximum energy is deposited in a shower is known as the shower maximum. Its depth can be parameterized with

$$t_{max} = 1.16\,[\ell n\,(E_\gamma/\varepsilon) - 0.62]\ .$$

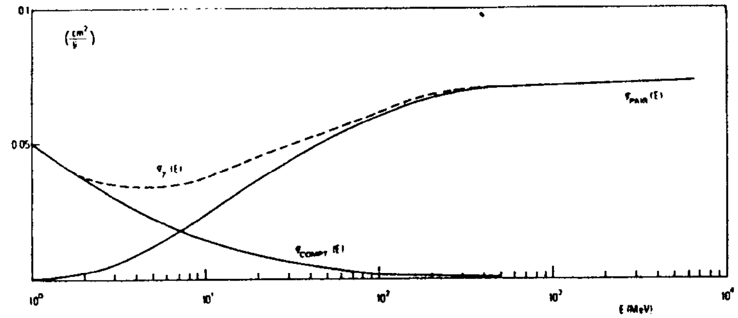

Figure 45: Energy dependence of the Compton and pair cross sections.

In the previous parameterization, t_{max} is given by $(a-1)/b$. EGS4 simulations give instead

$$t_{max} = 1.0\,[\ell n\,(E_\gamma/\varepsilon) - 0.5]$$

for electron showers, but

$$t_{max} = 1.0\,[\ell n\,(E_\gamma/\varepsilon) + 0.5]$$

for photons. The reason for the difference is that the photon shower starts approximately 1 radiation length deeper in the material because the photon must convert or compton to initiate the shower.

10.6 Landau Fluctuations

Often it is useful to know how the energy in a sampling layer will fluctuate. The shower usually consists of a large number of minimum ionizing particles, and the average energy loss is therefore rather well defined in any layer. Provided the number of particles or processes is large, the energy profile in that layer will be gaussian. But, if the thickness of the layer becomes small, or if the energy transfer is large, there will be larger fluctuations. A small probability, but high loss process will contribute a high energy tail to the gaussian distribution, as will the Poisson shape of a process involving small numbers of particles. The family of curves

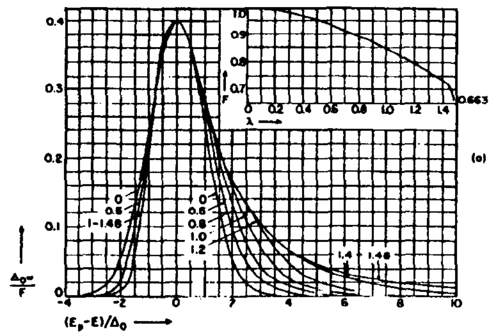

Figure 46: The Vavilov family of curves approaches the gaussian limit for $\lambda = 0$ and develops a tail for large λ.

describing this situation uses a parameter λ where $\lambda = 0$ represents the gaussian limit, and large λ represents a high energy tail. (See Figure 46)

The constant

$$\kappa = \frac{\xi}{\mathrm{E_{max}}}$$

is the ratio of the mean energy loss in an absorber to the maximum energy transferable in a single atomic collision [6]. Large $\kappa(> 10)$ implies a large number of processes, and a gaussian distribution. Small $\kappa(< 0.01)$ leads to the asymmetric Landau distribution [7]. The intermediate region of $0.01 < \kappa < 10$ is the most difficult to treat. Vavilov's theory of scattering [8] allows for an arbitrary ratio between large numbers of small energy transfers, and energy transfers near the kinematic limit, and has two limiting cases, namely, the Gaussian and the Landau distributions, [9], [10]. The GEANT manual has a typo in the discussion of these functions. The correct formulae are

$$E_{max} = \frac{2m_e c^2(\beta\gamma)^2}{1 + 2\gamma\frac{m_e}{m_x} + \left(\frac{m_e}{m_x}\right)^2}$$

$$\xi = 153.4(\mathrm{z}^2/\beta^2)(\mathrm{Z/A})\rho\delta\mathrm{x}(\mathrm{keV})\,.$$

As an example, let us calculate the requirement for a Landau distribution in Aluminum. We calculate that the mean energy loss (for heavy particles, not electrons) in 1 radiation length of Aluminum is 1.8 MeV. The maximum allowable energy transfer E_{max} will tend toward βp for large γ so the condition for a Landau distribution, $\kappa < 0.01$ becomes $\beta p > 180$ MeV. We will also get a Landau

λ in g/cm^2 and cm

material	$\lambda(g/cm^2)$	$\lambda(cm)$
Uranium	199	10.5
Lead	194	17.9
Copper	134.9	15.1
Iron	131.9	16.8
Aluminum	106.4	39.4

Table 3

distribution if the thickness of the material layer is small. For Aluminum, the parameter ξ is

$$\xi = \frac{180\mathrm{MeV}}{8.9\mathrm{cm}} = 20.2\mathrm{MeV/cm}\ .$$

For an incoming energy of 100 MeV and $\beta = 0.7$, the condition for a Landau distribution from a thin layer is given by the following:

$$\kappa = \frac{\xi}{\mathrm{E_{max}}} < 0.01$$
$$\xi < (0.01)(0.7)(100)$$
$$20.2\delta x < 0.7$$
$$\delta x < 0.035cm\ .$$

For intermediate energy, or layer thickness, the distribution will be a Vavilov distribution, and will approach a gaussian for higher energy or thicker layers.

11 Hadron Calorimetry

The transverse and longitudinal scale of a hadron shower is determined by the absorption cross section of pions instead of the interaction length in the material as it is for electromagnetic shower sizes.

The absorption length λ for several common calorimeter absorbers is shown in Table 3. Note that the scale of the hadron shower is larger than that for electromagnetic calorimeters by a factor of 33 for Uranium but a factor of 10 for Iron since $\frac{\lambda}{X_0} = 9.5$ for Iron and $\frac{\lambda}{X_0} = 32.8$ for Uranium.

The interaction length in the material is calculated from the inelastic part of the total cross section

$$\sigma_{inelastic} = \sigma_{total} - \sigma_{elastic} - \sigma_{quasi-elastic}$$

and is approximated by

$$\lambda_I \approx 35gcm^{-2}A^{1/3} \quad .$$

Inelastic cross sections, and therefore absorption lengths for neutrons, protons and pions are different, but the absorption length is usually tabulated for protons. Since a hadron shower is composed primarily of pions, the length which is most relevant for determining the longitudinal extent (and thus the required calorimeter thickness) of a hadron shower is the interaction length for pions. We can determine a rough correction for the tabulated values as follows. At 50 GeV, the pp inelastic cross section is about 33 mB, and the π p cross section is approximately 26 mB. This gives

$$\lambda_\pi \sim (1.2 \to 1.3)\lambda_p \ .$$

Many features of the hadron shower are similar to those of the electromagnetic cascade. For example, the shower depth grows logarithmically with energy, and the shower has exponential tails at the rear of the shower. The lateral size of the hadron shower is, however, significantly different from that of an electromagnetic shower. The scale is set by λ, but since some large fraction of the total shower energy transport is carried by soft neutrons which have low interaction cross sections, the shower is broadened. The shower tends to widen with depth up to the shower maximum where it begins to constrict again. (See Figure 47.) [11]

11.1 Hadron Calorimeter Resolution

When compared to an electromagnetic shower, more energy in a hadron shower is unsampled because of energy lost to neutrinos, energy lost to nuclear binding, saturation of heavily ionizing particles, and soft neutrons. The part of the shower which produces $\pi^0 s$, however, continues to generate electromagnetic showers. Fluctuations between the charged and neutral pion contents of the shower will lead to degraded resolution unless the electromagnetic and hadronic shower components have similar responses. To arrange for equality of response for these

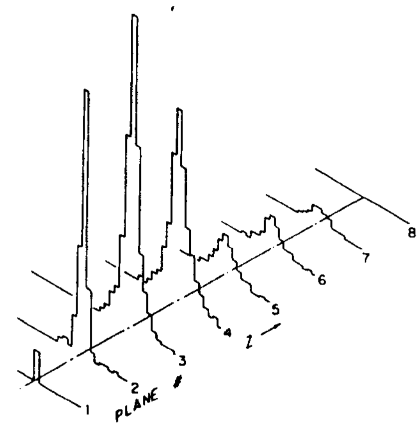

Figure 47: The shower profile widens with depth up to shower maximum.

components ($e/h \sim 1$), we must adjust the hadronic shower which has an absorption length which depends on A, ($\lambda \sim A^{1/3}$) and the electromagnetic shower which has a Z dependence.

$$X_0 \frac{dE}{dx} \sim \frac{1}{Z}$$

This match is nearly right for the elements Pb to Uranium, but for Iron, the e/h ratio is too high. The solution is to suppress the electromagnetic component. This can be accomplished by using thick sampling plates so that a larger fraction of the em energy is lost in the plates. This has several consequences. Iron will have a poorer energy resolution for electromagnetic components in a compensating calorimeter than would be possible in principle, and also, it may not be possible to achieve compensation in non-sampling, i.e., uniform devices like BGO. The effect on the device resolution of unequal response in the hadronic and electromagnetic shower components has been estimated by Monte Carlo to be approximately $(14\% \to 21\%)(1 - e/h)$.

12 Magnetic Field Shielding

For calorimeters with scintillator and photomultiplier tube readout, or for liquid argon devices with impedance transformers, external magnetic fields either due to external magnets which are part of a tracking detector, or even the earth's

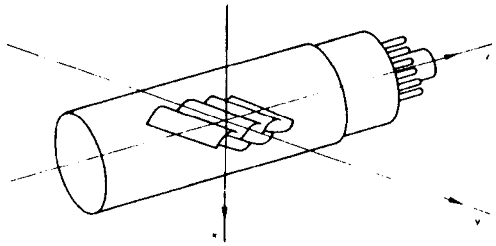

Figure 48: Sensitivity of Photomultipliers to external fields depends on the orientation of the tube relative to the field.

field, must be shielded to avoid gain shifts in the photomultiplier or saturation of the transformer core. For phototubes, a gain reduction of 50% is typical in fields of order 10's of millitesla (100 Gauss = 10 mT). The orientation of the tube relative to the residual field is also important, the tube being most sensitive to magnetic fields which are transverse to the tube axis and parallel to the plane of the multiplication structures, and least sensitive to fields along the axis of the tube. (See y axis in Figure 48.) Figure 49 shows the attenuation which can be achieved by using mu metal shields around the tube as a function of the ratio of the inner to the outer shield diameter. Typical reductions are of order 10^3 to 10^4. Attenuation of order 10^2 can be achieved for weak fields with Iron shields.

A more important magnetic effect in scintillators occurs because of a direct change in the light output of the scintillator when placed in a strong external field. Since the light output and spectra depend on atomic processes in the scintillator, they are affected by Zeeman splitting when a magnetic field is present. Thus, even if the phototubes for readout are properly shielded, one would expect to see a gain shift for a calorimeter operating in a strong field region. This effect is particularly important for calorimeters which try to achieve calibration accuracy below the 1% level. Test beam calibrations of submodules of a detector are often done, but in zero field conditions. It is difficult to imagine doing a full calibration complete with magnetic field since the field is typically a fringe field from a large magnet. Thus, the magnetic field effect must be calculated when using such test beam data. In the ZEUS detector, the calorimeters see the fringe field from the

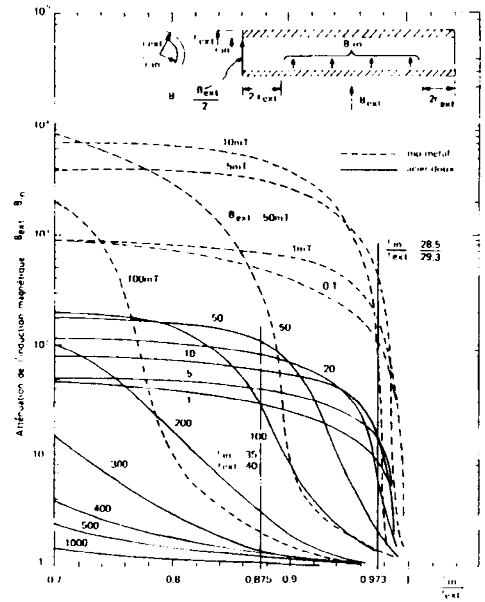

Figure 49: Attenuation of the magnetic field due to mu-metal shields as a function of the ratio of shield inner and outer diameters.

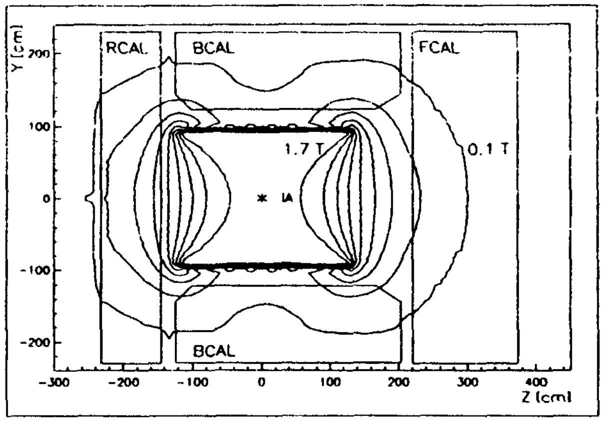

Figure 50: Magnetic field contours in the ZEUS calorimeter. The field steps are 0.2 Tesla.

main 1.7T superconducting solenoid. The fields range from 0 to 0.3 Tesla with local maxima as high as 0.8 Tesla. (See Figure 50 and references [12] - [13].) In the CDF detector, the endwall calorimeter calibration shifts by 5% when the 1.5 field is turned on, of which about 1% is due to changes in tube gain (as determined by light flashers) and the remainder is due to the scintillator [14]. For the ZEUS detectors, the aim is for a calibration accuracy of 0.25%, and the primary standard is the Uranium monitor current from the natural radioactivity. Figure 51 shows the variation in this calibration over a period of 5 days. The diurnal variation is due to the temperature coefficient of the tubes and bases. The light output from a ZEUS calorimeter submodule subjected to a magnetic field is found to rise rapidly by 1% between 0.0 and 0.02 Tesla. The light output is then stable up to about 0.1 Tesla, but rises 8% between 0.1 and 1 Tesla. The Uranium monitor current follows the light output up to about 0.3 Tesla, but does not show the subsequent rapid rise seen in the true calibration which is derived from an electron beam. Instead, it actually drops. This situation is somewhat disappointing because it makes the Uranium current more difficult to use for absolute calibration particularly because of the variation of the magnetic field itself over the module volume. See Figure 52

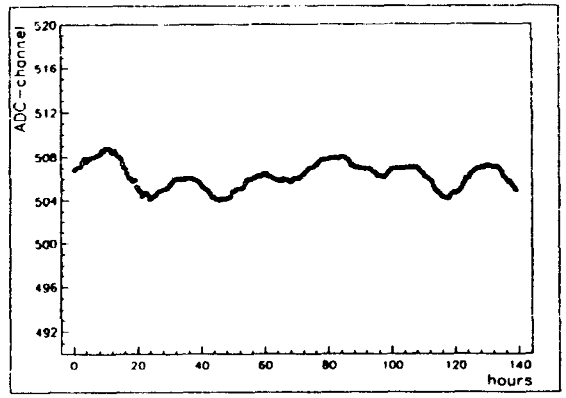

Figure 51: Time variation of the Uranium calibration signal over 5 days.

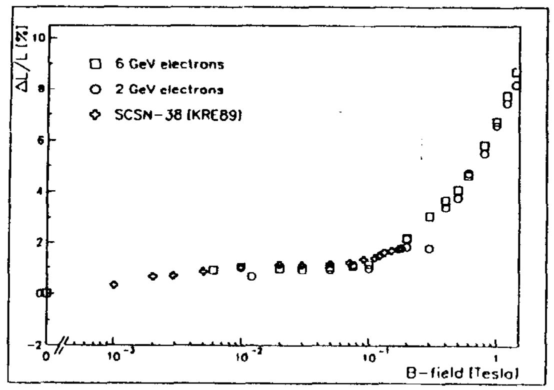

Figure 52: Calorimeter signal versus external B field.

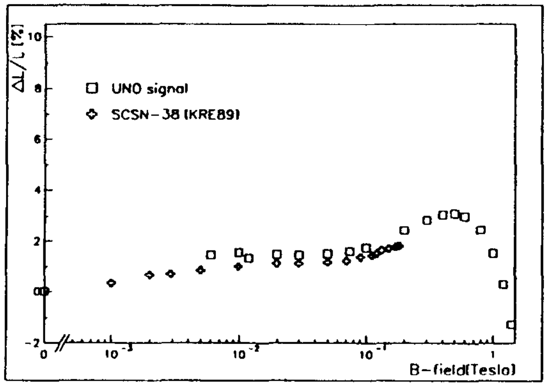

Figure 53: Uranium calibration signal versus external field.

and Figure 53 for a comparison of these yields.

You need to also be careful when using source calibrations for calorimeters with magnetic field on and off since the curling of beta or Compton electrons in the magnetic field can change the effective path length of particles from the source. In this case, it is, however, easier to simply compare a source calibration done with field on to one done with the field off.

13 Backing Calorimeters

Since the amount of energy left in a shower after 7 interaction lengths is small at today's energies, it is cost effective to consider replacing the main calorimeter with a cheaper design at that depth. This has been done in the ZEUS detector [15] calorimeter using 10 Fe plates, each 5 cm thick with Iarocci streamer tube readout. The resolution of this calorimeter for electrons and hadrons is approximately $70\%/\sqrt{E}$ and $90\%/\sqrt{E}$, respectively. Figure 54 shows the correlation between the energy deposited in the backing calorimeter, and the energy in the main calorimeter. Interestingly, the slope of the correlation is such that the response of the calorimeter to missing energy in the main calorimeter is slightly greater than its calibrated energy response. There are a number of possible explanations for this

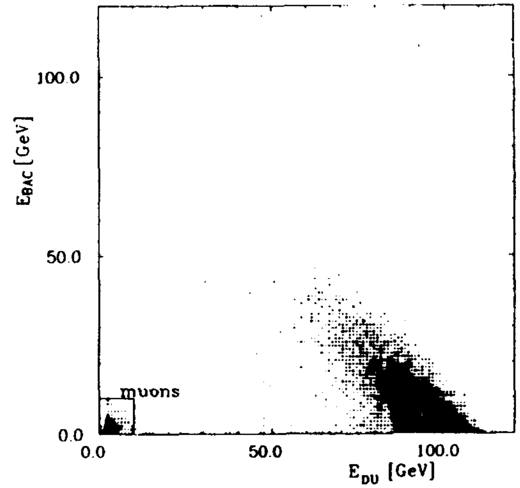

Figure 54: The correlation between energy deposited in the backing and main calorimeters for a 100 GeV hadron beam with some muon contamination.

effect including possible higher relative response to low energies in the backing calorimeters (non-linearities due to saturation, for example), higher relative response to low energy neutrons (which are more copious at the rear of the shower), or contributions due to side leakage.

The first and most obvious use of the backing calorimeter is to improve the energy resolution of the main calorimeter by adding the two measured energies. An even better technique is to restrict the sample if possible to those events whose showers leave less than 1% of their energies in the backing calorimeter. These showers are measured with much better precision than the average. Figure 55 shows the effect of using the backing calorimeter for 50 GeV hadrons. The resolution of the calorimeter is $41\%/\sqrt{E}$ with no cut on the backing energy fraction and $36\%/\sqrt{E}$ with a 1% cut.

A much more important result of using a backing calorimeter is its effect on missing energy resolution. A large portion of the tail on the resolution in missing energy is caused by showers which begin deep within the calorimeter and therefore

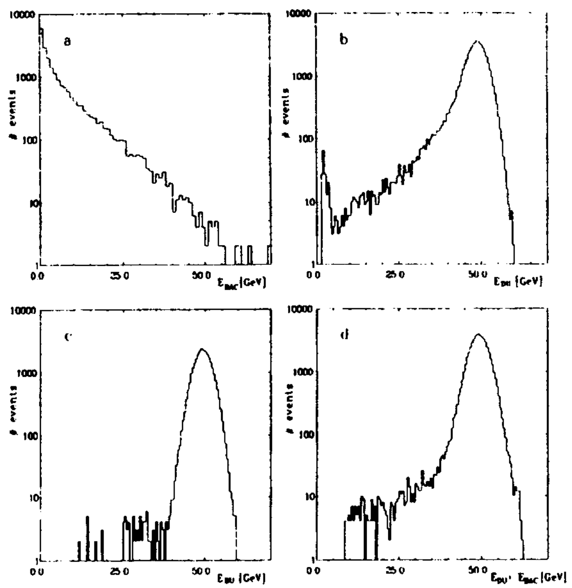

Figure 55: The distribution for 50 GeV hadron showers of backing energy a), main energy b), main energy after a 1% cut on the backing energy c), and the total energy d).

have large leakage corrections. The use of the backing calorimeter for the ZEUS detector reduces the tail on the missing Et from 7.6% to 0.5%. Thus when used in this way it substantially improves the resolution in missing energy.

13.1 e/h = 1

The hadron shower has four main components.

Electromagnetic showers from π^0 and η

Ionization loss from charged hadrons

Nuclear excitation and breakup

Soft Neutrons (primarily below a few MeV)

The resolution of the calorimeter will depend on the fluctuations and also the correlations between each of these shower components. The effect of fluctuations on the overall resolution can be minimized by having an equal and linear response to each of the shower components. In particular, in order to equalize the response to the large fluctuations between the electromagnetic and hadronic components, we would like to require $e/h = 1$, i.e., a balance between the response to an electron, and that for a hadron of the same energy.

It has now been realized that the neutron component of the shower plays an important role in determining the e/h ratio via the interaction of soft neutrons with protons in the detection medium [17], [18]. The resulting soft scattered protons can produce large signals due to their heavy ionization. Saturation or recombination of the ionization in the medium will reduce this effect. The signal integration time can also affect the e/h value since the soft neutron component of the shower develops slowly. Thicker absorber layers, or lower Z values can also be used to adjust the e/h value by suppression of the electromagnetic response. Several configurations were investigated by the ZEUS group to determine the effect of non-compensation on the calorimeter resolution [19].

The values in Table 3 show that there is a modest increase in the resolution of the detector at low energies for a 10% change in e/h (compare, for example, the

Setup	Energy	Electron $\sigma/\sqrt{E}$	Hadron $\sigma/\sqrt{E}$	e/h
T60A1	3	0.121	0.527	1.36
	8.75	0.137	0606	1.34
T60A2	3	0.157	0.401	1.13
	8.75	0.157	0.418	1.10
T60B1	10	0.173	0.384	1.00
	50	0.197	0.4d14	1.01
T60B3	10	0.176	0.351	0.95
	50	0.186	0.353	0.95

Table 4: Configurations tested by the ZEUS collaboration to investigate the effect of e/h on calorimeter resolution.

setup	A	B	e/h
T60A2	0.398	0.041	1.13
T60B1	0.376	0.018	1.00
T60B2	0.360	0.010	1.01
T60B3	0.345	0.010	0.95

Table 5:

A2 and B1 results). But to see the real importance of the effect, one should fit the resolution to the form

$$\frac{\sigma_E}{E} = \frac{A}{\sqrt{E}} \oplus B$$

The results shown in Table 5 demonstrate that there is a very significant effect on the high energy limit of the resolution (B) (- over a factor of two between A2 and B1). Thus, even though the effect on the resolution is small at low energies, it may become important for a calorimeter attempting to achieve optimum energy resolution at high energies.

The original motivation for using Uranium in hadron calorimeters was the hope that the shower would induce fission in the Uranium, and that the resulting conversion of the usually lost nuclear binding energy component of the shower would be partially recovered in an observable way, thus improving the resolution. The first Uranium scintillator calorimeters did in fact have improved resolution, but subsequent results on different types of calorimeters could not be clearly interpreted with the above model. Work by R. Wigmans with shower monte carlos showed that the intrinsic resolution of the hadronic detector is dominated by fluctuations in the binding energy losses occurring in the nuclear reactions, and that the neutron flux in the shower which is large, is strongly correlated with these losses. Free protons in the sampling medium improve the detection of these neutrons since maximum energy transfer occurs when $m = m_n$. The soft protons are amplified by their heavy ionization which goes as $1/\beta^2$.

14 Monte Carlos

A large number of monte carlo programs now exist which can be used to evaluate the importance of the various components of the showers and to estimate the expected resolution for a particular calorimeter material. Some like CALOR [20][21] [22], MORSE [23], and EGS [24] (electromagnetic showers) are descendants of code which was originally used for radiation shielding calculations. Others like HETC[25], FLUKA [26], NEUKA, (FLUKA plus fast neutron and EM transport) and GEANT [27] were designed for calorimeter and detector calculations.

14.1 NEUKA

One monte carlo which has been used heavily for HERA and which illustrates a number of features of similar codes is NEUKA [33]. Since hadron transport codes can be notoriously slow due to the large number of particles in the hadron shower and the large number of processes and cross sections which need to be calculated, the goal of this monte carlo was to obtain significant speed-up but still maintain the correlations between the fluctuations in the different components of the shower. Starting from the FLUKA monte carlo, the neutron and EM transport codes were simplified. The radial electromagnetic shower distribution, for example, is parameterized with

$$f(r) = 1.1e^{-2.28r} + e^{-0.635r}$$

where r_e is measured in Moliere units. The longitudinal distribution is given by

$$f(z) = z^a \exp(-bz)$$

where z is the depth measured in radiation lengths. The a and b parameters of the longitudinal distribution are given by

$$a = 2.0 - Z/340 + (0.664 - Z/340)\ell n E$$

$$b = 0.634 - 0.0021Z$$

where Z is the material atomic number. (See also J. del Peso and E. Ros for a description of a detector specific fast monte carlo.) [28]

The speed-up of a factor of 20-40 which was achieved provides a much more useful tool for investigating quickly the effect of changes in the detector design, and provides a more useful code to use as the basis of a simulation program for physics processes, calculations of efficiencies and acceptances, and studying the feasibility of different physics analyses.

The NEUKA code preserves the detailed simulation of the basic processes in the hadron shower, but simplifies the transport of neutrons and the development of electromagnetic showers, and the approximations need to be verified. To do this, a mock-up of the calorimeter was exposed to beam, and instrumented with dosimeters. The calculated yields of isotopes in the monte carlo can be compared with the activation yield measured by the dosimeters. Figure 56 shows a comparison of the calculated and measured yields which agree quite well.

Once the monte carlo has been verified, it can be used to extract useful information about the shower. The monte carlo indicates that the neutron component of the shower is measured with a surprisingly high accuracy of $9\%/\sqrt{E}$ due to the large fraction of neutron energy which is deposited in the scintillator. The charged component of the hadron shower is measured with a resolution of $15\%/\sqrt{E}$ as is the electromagnetic part of the shower. This is, however, a coincidence since the pions are measured with 9% resolution, and the protons with only 27%. This poor proton resolution may be due to the fact that most of the protons originate from nuclear processes and are very soft, often stopping within a single absorber plate.

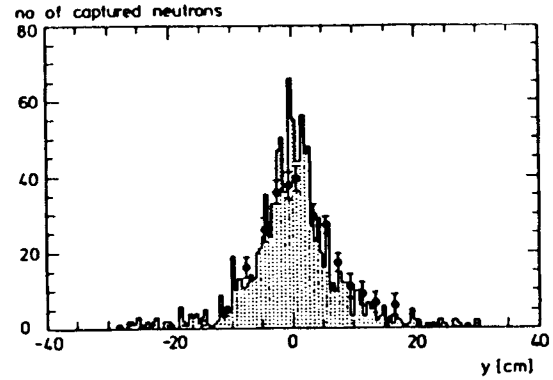

Figure 56: Comparison of the transverse distribution of activation computed in the NEUKA monte carlo, and measured in the dosimeters.

14.2 Monte Carlo Resolution Calculations

The monte carlo can also be used to study the intrinsic resolution of the calorimeter. The signal from the calorimeter can be thought of as consisting of a sampled fraction of the neutron shower, the ionization losses in the scintillator, and a sampled fraction of the electromagnetic shower which, however, has perhaps a different gain factor due to the different response to an electron when compared to a minimum ionization loss.

Using the monte carlo, one can investigate the consequences of not measuring the neutrons by removing this component of the signal. The 10 GeV calorimeter resolution changes from $30\%/\sqrt{E}$ to $60\%/\sqrt{E}$ when this is done. There is a strong energy dependence, with a 95% figure expected at 100 GeV. (See Figure 57.) The 60% resolution obtained at low energies agrees reasonably with the typical resolution achieved in early non-compensating calorimeters. With neutrons included, the prediction is a $30\%/\sqrt{E}$. This underscores what has been learned in the past few years, that is, the neutrons are an extremely important part of the shower process. One can also investigate with this tool the origin of the difference (slightly more than a factor of 2) between the best achievable electromagnetic resolution, and that obtained for hadrons. Most of the problem with the hadronic resolu-

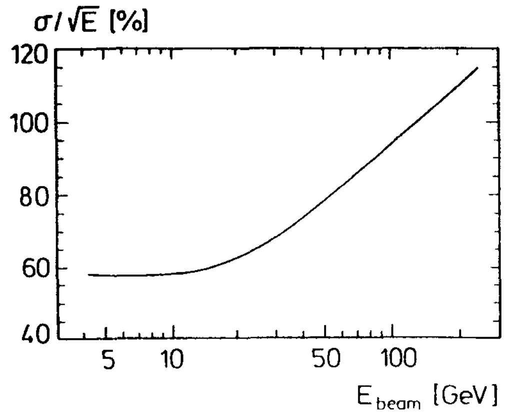

Figure 57: Expected pion resolution without neutrons for a ZEUS structure of infinite thickness. NEUKA monte carlo.

tion appears to be that different types of energy have quite different detection efficiencies. The monte carlo indicates a 3.5% efficiency for nuclear excitation energy, 4.5% for electromagnetic energy, but 7.31% for charged pions and 7.6% for protons. Despite this rather good average detection efficiency, the proton energy resolution is quite poor. Thus, the combination of the different efficiencies, with the fluctuations in the shower components and the poor soft proton resolution leads to substantially poorer resolution seen in hadron calorimeters. Future calorimeter designers will be able to use these types of calculations to vary the shower detector's material thicknesses and composition in order to achieve better balance in the detection efficiencies and thus improved resolution.

Neutrons have a large mean free path in the calorimeter material, so they increase the apparent lateral and longitudinal size of the shower. A $\sim$ 2 MeV neutron, for example, has a range of 6.6 cm in Hydrogen and 11.8 cm in Carbon. In addition, Hydrogen damps the development of the neutron cascade acting like a neutron moderator. The average energy of the neutrons involved in the cascade is of order 0.5 GeV. As we have seen earlier, the neutrons will also affect the time structure of the pulse in a calorimeter since they are absorbed slowly. In fact, in calculating the degree of compensation achieved, it is important to include this effect since some of the neutron induced signal may fall outside of the electronics gate used to collect the pulse. In Uranium, 90% of the neutrons are captured within 400 ns due to the high neutron cross section. In Lead sampling calorimeters, however, the same collection might take 8 to 15 microseconds for sampling thicknesses between 0.33 and 1 cm [28].

14.3 Neutrons in gas detectors

In general, neutrons can be problematic for gas sampling detectors. Studies [29] have shown that the response of gases to neutrons depends strongly on the proton content as expected and that while the $e/h = 1$ condition can be achieved, it does not lead to significantly improved resolution. Large non-gaussian fluctuations in the shower response are generated with the addition of hydrogen, and the spatial extent of the shower is considerably increased. The neutron signal is infrequent but large and subject to large fluctuations so the overall conclusion is that the attempt to detect the neutrons leads to poorer overall resolution.

15 The CDF Central Calorimeter

The CDF Calorimeter is the calorimeter with which I am personally most familiar. It was built some time ago, so it does not represent the most modern construction techniques, and there are several things which would be done differently if it were to be reconstructed. Nevertheless, it is one of the few examples of a running, large scale calorimeter and, in particular, the only running hadron calorimeter at a hadron collider, so it is useful to study its performance.

The central electromagnetic calorimeter is constructed from 48 azimuthal modules which are each divided into 10 theta (η) towers. The calorimeter is actually 4 separate sections in the form of half cylinders using 12 modules each. These subcylinders can be retracted when it is necessary to repair or service the detector. The electromagnetic calorimeter is mounted directly on the front of the hadronic calorimeter which has the same mechanical structure.

The electromagnetic section is 18 radiation lengths thick, and consists of 20-30

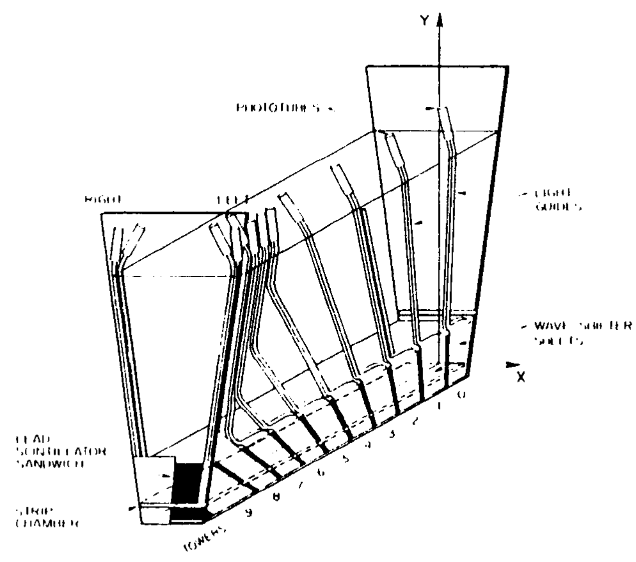

Figure 58: Light guide system for the CDF electromagnetic module.

layers of lead and 21-31 scintillators depending on the η position. The scintillator is SCSN-38 polystyrene and the absorber 1/8 inch Aluminum clad lead. Light is collected using wavelength shifters (see Figure 58) of UVA acrylic with 30 ppm Y7 dye. There is a gap at 5.9 radiation lengths (including the coil) near shower maximum containing strip chambers which are used to determine the position of a shower and to measure its transverse profile. This technique is extremely important for electron identification since an accurate position measurement can be used to eliminate electron candidates which arise from the random overlap of an energetic pizero with a charged track, and the transverse shower profile can be used to reject hadron showers as well as conversion pairs. Each strip chamber has 64 wires and 128 strips and has a physical thickness of 0.75 inches and 0.069 radiation lengths. The position resolution of the electromagnetic calorimeter is $13\%/\sqrt{E}$ with a $1/\sqrt{\sin\theta}$ angular dependence. The position resolution of the system together with the strip chambers is approximately 2 mm.

15.1 The Hadron Calorimeter

The hadron calorimeter is also divided into 48 modules, but there are only 6 towers in the η direction. The resulting segmentation is $\Delta\phi, \Delta\eta$ = 15 degrees, 0.11. The depth is 4.5 interaction lengths since the module is constructed from 15 layers of 5 cm steel, each followed by 1 cm of scintillator of the PMMA type. Each tower and layer requires a different size piece of scintillator, but the average dimension is 1 x 35 x 70cm.

Since the anode current in the PMT's reading out a calorimeter at a bunched collider like the Tevatron changes significantly between pulses and also as a function of luminosity, it is necessary to ensure that the gain (i.e., calibration) of the detector does not vary due to this effect. Each phototube used in the construction was tested for gain stability as a function of anode current, and for further stabilization, the photocathodes are illuminated with green light prior to passage of the beam bunch which produces a stable peak anode current of 100 nA. The absolute output of individual plates of scintillator which vary in size and shape was corrected for by matching individual towers with light guides of varying attenuation and by inserting correction filters between the wavelength shifters and the light guides.

15.2 Monitors for Calibration

Laser light is distributed via fibers to all of the calorimeter phototubes. The distribution system uses several neutral density filters which can be used to check the linearity of the system and fibers to bring the light to the detector. Every 13th fiber in the detector light distribution system goes to a set of 4 reference tubes held in a temperature controlled box which also contains NaI crystal light monitors. In addition to the light monitor system, a Cs137 source can be moved at constant speed and fixed longitudinal depth through the detector, and a line source can be used which is positioned along the edge of a module but in the center of a tower. Figure 59 shows the results of Cs137 source runs. Certain regions of the detector require more detailed relative calibration information which can only be obtained from test beam studies.

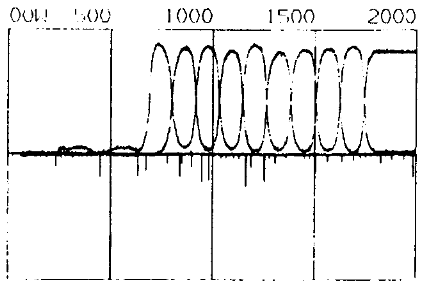

Figure 59: The output of the Cs137 calibration showing the individual photomultiplier currents as the source travels through a module. One trace is the sum of all phototubes, and the second is the odd phototubes only.

As shown in Figure 60, some of the regions between submodules can be physically complicated, but, for a complete simulation as well as a good understanding for later physics analysis, it is essential to know how the calorimeter responds in these regions. Information of this type needs to be incorporated into the detector simulation package, and it needs to be available so that regions may be excluded from certain analyses, or corrections can be applied to the response function.

15.3 Cluster Finding

It doesn't do much good to have constructed a great calorimeter if the software for analysis cannot determine which energy deposits to add together. This can actually be quite a complex task, and may need to be re-optimized for different types of physics analyses. The resulting "cluster finder" can have a significant effect on the achieved resolution of the calorimeter when used in a real experiment. For example, it is necessary to determine how much of the transverse extent of a shower should be added to the central core energy deposit. If you add too much, you will pick up additional noise from the calorimeter as well as "noise" from energy deposits due to other jets or other particles as well as the minimum bias "fizz." If you include too little, shower energy will leak out and the resolution will be degraded. In addition, if the physics process of interest requires the detection of particles or jets which are on average close together, the optimum may be

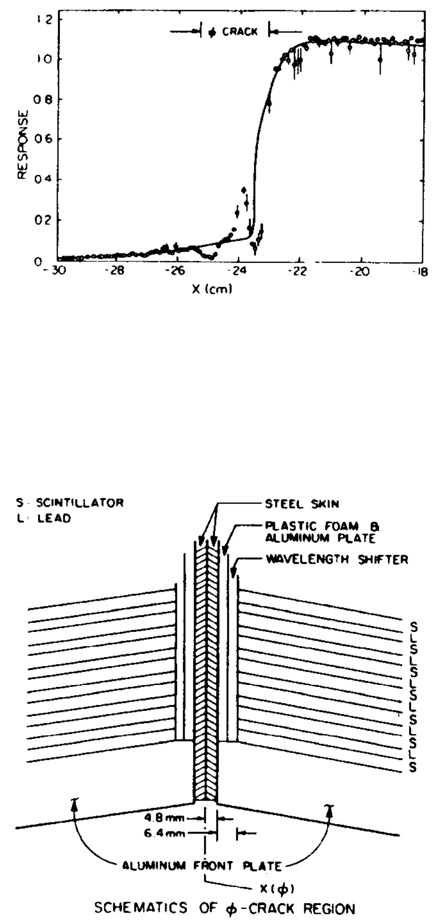

Figure 60: A comparison of the test beam response and the physical construction in the crack region between modules.

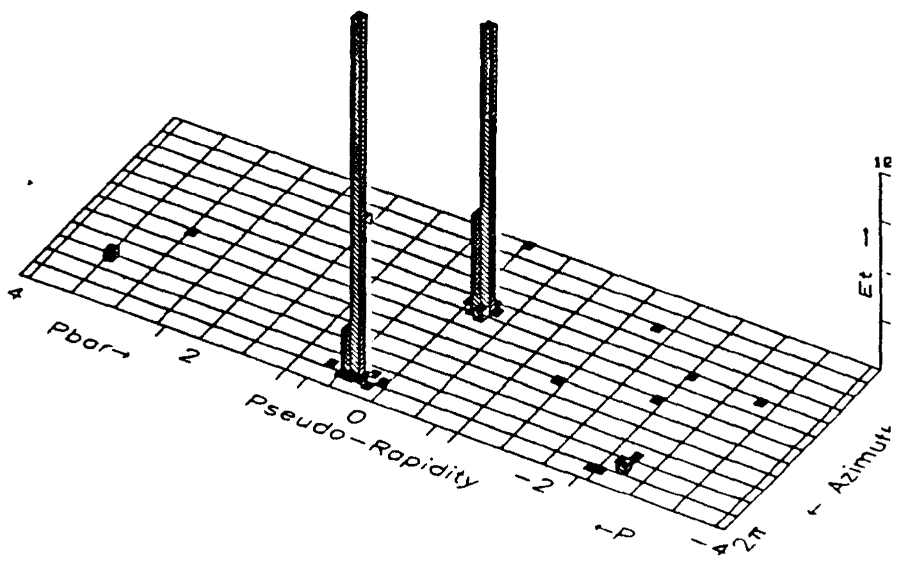

Figure 61: A simple two jet event with well separated energy deposits presents little problem for the cluster finder.

different from that used for well isolated energy deposits. Cluster finding can also affect the absolute calibration scale since it changes both the average amount of leakage and the minimum bias contribution. All of this indicates that significant effort must go into the design and study of the clustering algorithm. Most present algorithms add all of the energy found in a cone of fixed size. To some extent, this is done to simplify the comparison of the experimental results with theoretical calculations. But even with a fixed cone size algorithm, there are generally several other important parameters. For example, there are parameters which determine when showers need to be merged together, thresholds which indicate the presence of additional nearby energy, and criteria for locating seed clusters which initiate cones, and even parameters to determine how to center the cone itself.

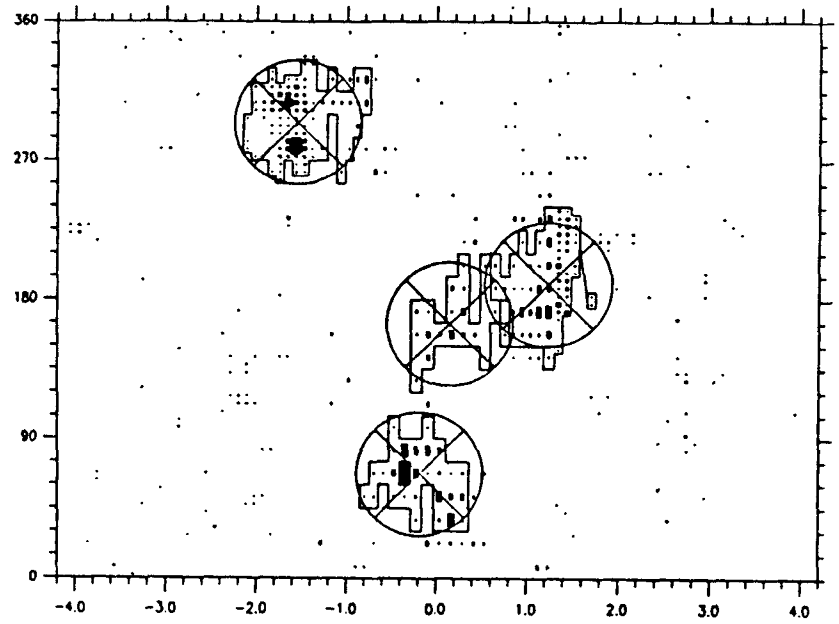

Figure 62: A four jet event in CDF shown on the $\eta\phi$ plane, presents more complex problems for cluster finding (see text).

As shown in Figure 61, a simple two jet event rarely presents a significant challenge in cluster finding at today's energies outside of the question of its effect on the energy scale and calibration. A four jet event such as that shown in Figure 62 presents several complex issues. In the event shown, the small squares represent energy deposits above 0.5 GeV. The size of the square is proportional to the transverse energy, and circles indicate jets found by a fixed cone size (0.7) algorithm. Notice the almost uniform scattering of energy across the $\eta\phi$ plane coming from the underlying event. Some subtraction for this effect should be made from the energy found in the cone. One might also consider whether the two central jets should in fact be merged, or if not, how should the energy be apportioned between the resulting clusters. For the top cluster, one suspects that this may be two distinct energy depositions, but perhaps it is merely a jet with two energetic particles. All of these issues need to be addressed by the cluster algorithm.

15.4 Absolute Calibration

In recent measurements by the CDF collaboration of the W and Z masses, the absolute calibration of the calorimeters was a critical issue. In determining this calibration, the tracking detectors were calibrated both at low and at high momenta by using the copiously produced J/Ψ and the Upsilon. Both checks used the decay to two muons to minimize corrections for final particle interactions. An example of the dimuon mass spectrum obtained in this way for the Ψ is shown in Figure 63. This calibration of the tracking momentum scale is then extended to the electromagnetic calorimeters by using a clean electron sample with well isolated tracks (primarily from B meson decays) to compare the measured electron energy and tracking momentum. The E/P distribution should peak at a value of 1.0 with a small radiative tail. Radiated photons tend to be collected in the same region as the primary shower, and hence E remains unchanged, but the track momentum is underestimated which leads to the distribution shown in Figure 64. These techniques cannot be extended in a simple way to the hadron calorimeter. An isolated sample of high energy pions could be used to check the e/h ratio, but in this calorimeter in particular, e/h is not expected to be 1.0 nor is it constant with incoming particle energy. While it is desirable to have a calorimeter where $e/h = 1$ on average in a shower, the e/h ratio is momentum dependent particularly below a few GeV. Further, single, isolated, high energy pions are relatively rare, and not usually part of the trigger. This means that the absolute scale for the hadron calorimeter relies to a greater extent on the calibration systems. As we will see later, there is some ability at the SSC to use the copious production of W's and Z's and their decay into jet pairs to constrain the calorimeter scale.

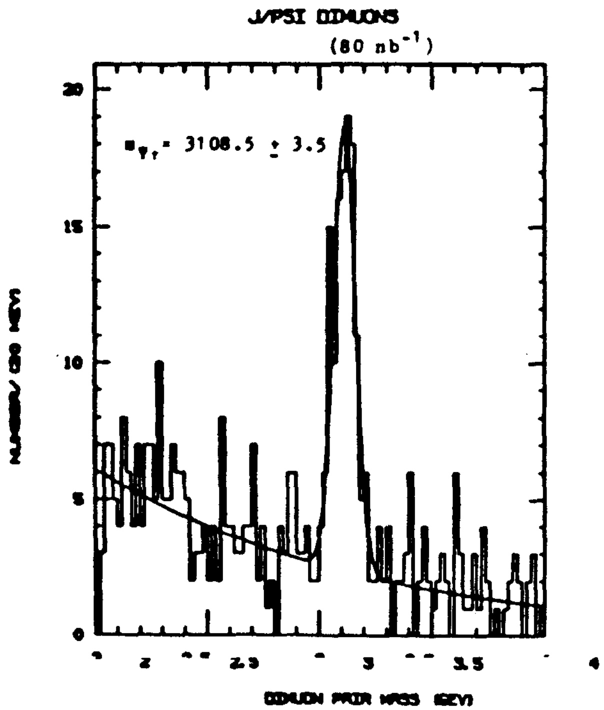

Figure 63: Determination of the Ψ mass using dimuons. Only a small portion of the CDF sample is shown.

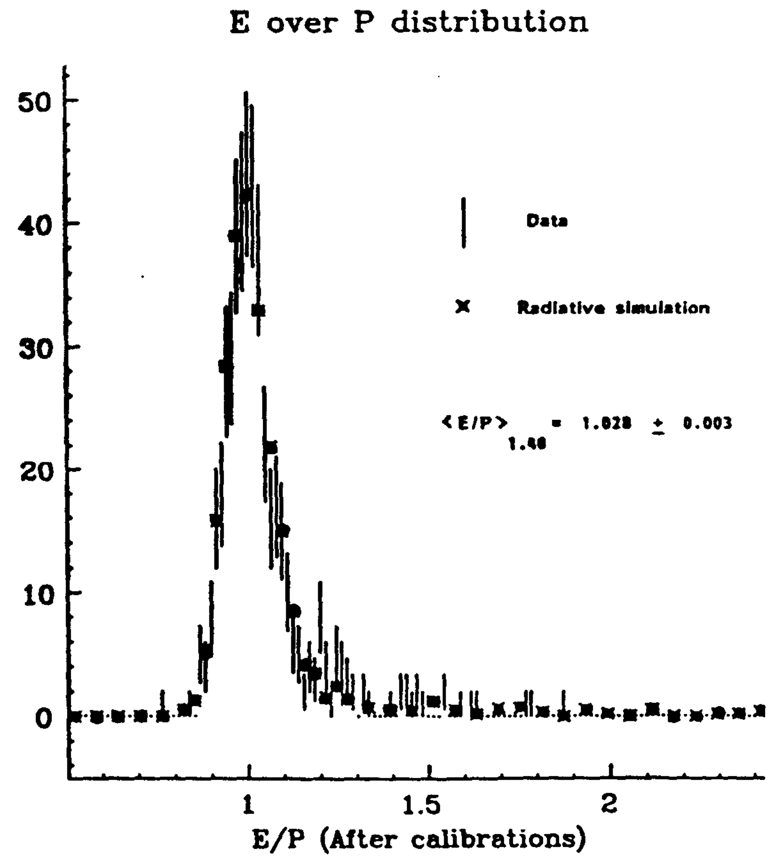

Figure 64: The E/P distribution compared to a simulation of the shape expected including radiative effects.

16 Ionization Calorimetry

A large number of experiments including R806, Mark II, SLD, D0, E706, E653, Helios, Venus, and H1 at HERA have included calorimeters in their detectors where the signal in the sampling layers depends on the collection of primary ionization produced by the charged particles in the shower. This technique has in most cases relied on the use of Liquid Argon as a sampling medium though attempts have been made in recent years to produce similar results with non-cryogenic liquids. The advantages of this technique are that it is relatively radiation hard, produces a detector with good uniformity across tower surfaces, can be easily segmented into as many towers as needed, can accommodate the small segmentation necessary for electromagnetic detectors, it is very linear, and has extremely good calibration stability. The final point is probably the most important, and comes about because the signal strength depends only on the physical characteristics of the ionization process provided there are no losses of signal due to impurities in the liquid. The VENUS (Tristan) detector, for example, achieved $11.3\%/\sqrt{E} + 1.4\%$ resolution **without** calibration.

The disadvantages of the technique in Liquid Argon are the slow charge collection, the need for a cryostat, lack of compensation, and noise performance. The presence of the cryostat makes the design of the remainder of the detector more difficult, particularly near the ends of any central calorimeter.

16.1 Readout Speed

The charge collection time in Liquid Argon which is approximately 200 ns per mm of sampling gap limits the ultimate speed of this type of calorimeter. Measurements have, however, shown that this can be improved to as small as 50 ns per mm with the addition of 1% Methane. This problem of readout speed for ionization devices has been studied by Radeka and Rescia who showed that the detector capacitance and cable lengths can also have a significant effect. They found that the detector rise time, for example, would be given by

$$t_r \approx 3.6(C_D L_s)^{1/2} \approx 3.6 T_D \left(1 + \frac{C_D}{C_C}\right)^{1/2}$$

where C_D is the detector capacitance and C_C, L_s, T_D are the cable capacitance, inductance and delay. As an example, for a cable delay of 7 ns and a cable capacitance of half the detector capacitance, the rise time would be 43 ns. Actually 7 ns delay on the cable may be close to a minimum due to the physical size of a hadron calorimeter. Solutions to this problem require low inductance signal lines or increased longitudinal segmentation. Note that the rise time in nanoseconds is about 40 times the cable length in meters.

Ionization detectors work at very small signal levels, and therefore have higher noise per tower than a scintillator calorimeter. SSC studies for the SDC group indicated a noise level of order 1 GeV in a cone of $\Delta R = 0.15$ including pileup contributions from multi events within the measurement time (roughly 2 times the rise time) at a luminosity of 10^{33}. This has implications for the minimum usable hadronic energy deposit and for cluster finding, but the effect is less severe than might be imagined at first because of the intrinsic hadronic noise coming from minimum bias events which provides similar limitations for scintillator.

16.2 Compensation

Compensation in liquid ionization detectors is still somewhat of an open issue. SLD, for example, measured $e/\pi = 1.24 \pm 0.1$ at 11 GeV for a 2.76 λ iron backed calorimeter. This can be converted to e/h using [30]

$$(e/\pi)^{-1} = 1 - (1 - h/e)E^{(0.14)}$$

where E is measured in GeV. This represents an e/h value of 1.37 and a constant term in the resolution which one would estimate from previous discussion to be $0.14(1-e/h) = 5.2\%$. The D0 and Helios groups, on the other hand, find $e/h \sim 1.1$ [31].

An alternative method of achieving compensated response in the calorimeter has been investigated for calorimeters which have large numbers of longitudinal segments. Since, as discussed earlier, the composition of the shower changes gradually with depth, by weighting the energy at different depths unequally, a correction can be made for unequal response to the various shower components. The technique involves using test beam data to optimize the detector resolution as a function of the weighting factors. One can also imagine taking advantage of possible correlations between energy samples for a detector with fine longitudinal segmentation. This type of compensation will be used in the H1 Liquid Argon detector.

16.3 Warm Liquids

Recent results of the WALIC collaboration, and previous work by the UA1 collaboration have demonstrated the feasibility of using chemicals which are liquids at room temperature as a replacement for cryogenic liquids like Argon.

16.3.1 Electrostatic Transformers

An important technique for reducing the detector capacitance to improve noise performance is provided by what is called an electrostatic transformer. In liquid ionization detectors, magnetic transformers are often used to provide impedance matching between the large stack capacitance and the amplifier input. A similar matching can be achieved if the detector capacitance is reduced by connecting signal gaps in series rather than the usual parallel arrangement.

A module of this type which was constructed at LBL and tested at Penn is shown in Figure 65. The absorber plates are split, with one side being at high voltage and the other at virtual ground. A thin sheet of kapton separates the two plates and also forms a high capacitance bypass capacitor which leads the signal toward the central plate where it is extracted at virtual ground. It is important to note that while the electrostatic transformer technique reduces the AC capacitance of a detector stack by $1/\sqrt{s}$ where s is the number of gaps placed in series, the DC capacitance of the module remains unchanged and large. Good noise performance requires a high pass filter in the amplifier.

17 t Quark Mass Measurements at the SSC

As a final illustration of the use of calorimeters in the future, I would like to use the precision measurement of the t quark mass at high energies, since it illustrates

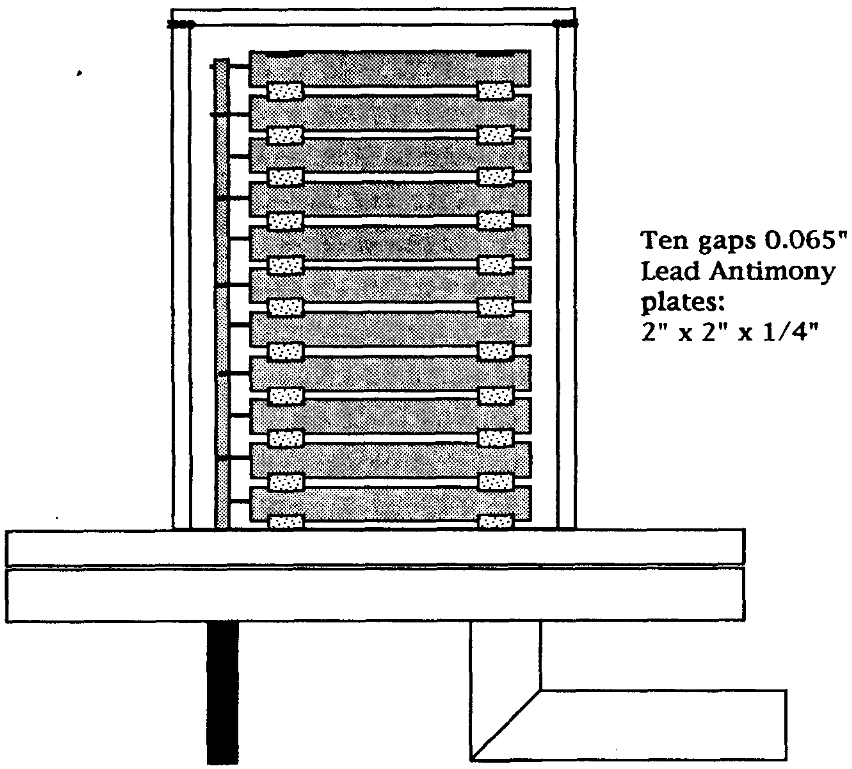

Figure 65: Module using electrostatic transformer techniques constructed at LBL and used in TMS at Penn.

many of the requirements placed on the entire calorimeter system [32]. The problem is the following: If the t quark mass is light on the SSC scale (say 130 GeV), it is copiously produced at the SSC and may well represent a significant background for many signatures of new physics. This copious production, however, provides an opportunity to measure the t mass to high precision.

The typical decays of a heavy top would be $t \rightarrow Wb$ with subsequent decay of the W to leptons or quark pairs. For an event with a t-tbar pair, the branching fractions are 44% purely hadronic states, where both t and tbar quarks decay into lighter quark pairs, 15% semileptonic for one quark for each of the leptons, and 1-2% double semileptonic. The purely hadronic decays lead to 6 jet final states, but the background from QCD is extremely high. For the single semileptonic decays, only the e and μ modes are usable. The double semileptonic decays provide a low rate but clean final state for top quark detection. The presence of two energetic neutrinos, however, limits the achievable mass resolution for the t quark. The chief background for the most promising single semileptonic mode is W plus multijet production.

At the SSC, for a light t mass, the event rate is high, so it is possible to design cuts which optimize the signal. The object is to detect a lepton plus missing energy from the t or tbar, and to reconstruct a W into two jets mode for the other t quark. This detection of two W's significantly reduces the W plus jet background. The reconstruction of a W in the hadronic mode at present energies is known to be difficult in the case of inclusive W production due to inadequate calorimeter resolution and high QCD backgrounds. In this case, the lepton plus missing Et helps reduce QCD backgrounds. To improve the hadronic resolution, we have seen that we should expect resolutions between 30% and 60% over $\sqrt{E}$. Thus by requiring high Pt for the individual jets, the resolution can be improved up to the point where it is limited by constant terms in the resolution. This later limit will in turn depend on the degree of compensation in the calorimeter and the calorimeter's uniformity and inter-module calibration stability.

The selection of two very high Pt jets will assist in the W detection. To further constrain the events to contain objects likely to come from t decays, we assume that it will be possible using a vertex detector to tag two b quarks with identified

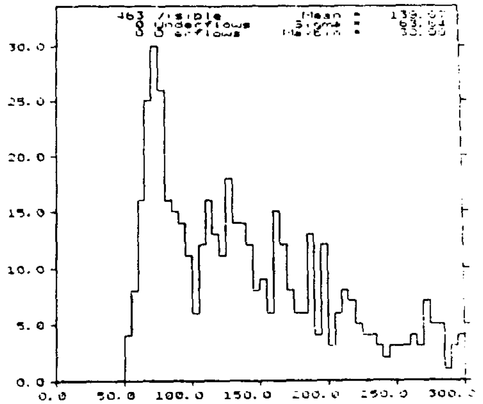

Figure 66: Two jet invariant mass distribution for events with two b vertices and Pt - jet > 120 GeV.

vertices. This further reduces any QCD background, and if the identified b jets are not used in the W reconstruction, it also reduces the combinatorial background in the W mass reconstruction. Figure 66 shows the invariant mass distribution for events where two b vertices have been found, when the Pt cut used on the individual jets is 120 GeV, and the jet cone size is a relatively standard 0.7. A further increase in the jet Pt threshold should improve the resolution, but as can be seen from Figure 67, this does not happen. Instead, the signal almost vanishes because, with this Pt requirement, the average Pt of the W becomes high enough so that both jets fall within the cone of 0.7. They are still separable, however, because of their very high energy.

By using a different clustering algorithm, one obtains the jet pair mass distribution shown in Figure 68. The shaded region contains the W's, and the central mass has been shifted downward due to the lack of a correction in the clustering for the ratio of the incoming jet energy to the detected energy. No attempt has been made yet to optimize these corrections. To measure the top mass, the reconstructed W must be combined with one of the tagged b jets. The resulting mass distribution in Figure 69 shows that it is possible to reconstruct the t with good

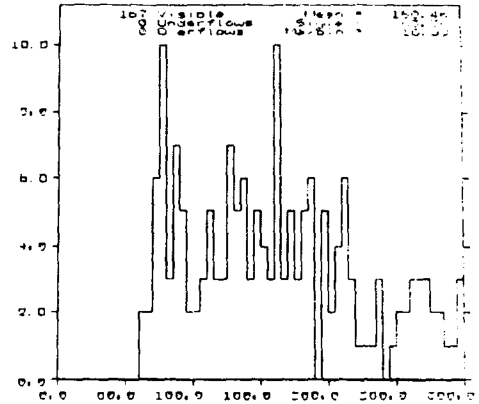

Figure 67: The invariant mass distribution using a cone size of 0.7 and a Pt cut of 180 GeV.

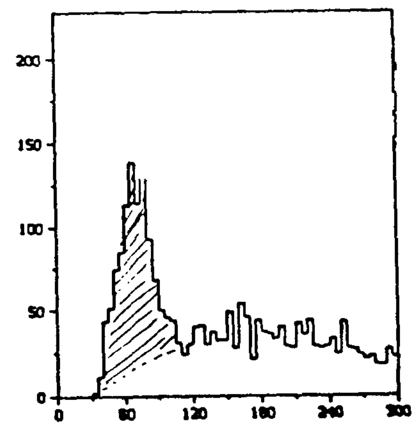

Figure 68: Jet pair distribution for Pt > 180 GeV. The shaded region contains the W.

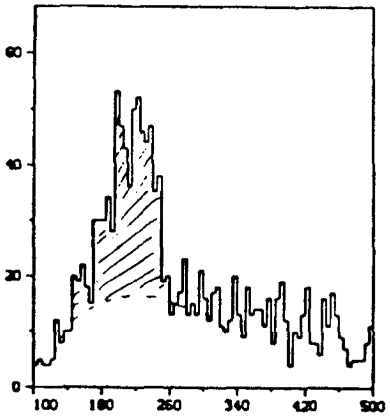

Figure 69: Reconstructed top quark mass from W,b pairs where the W jets have Pt > 180 GeV.

resolution. The t quarks in this case had a mass of 250 GeV, and the largest systematic error in the method is due to the correction of 30 GeV which results from the scale shift between jet energy and detected energy. Most of this shift should in principle be removable if the jet pair which constitutes the W is constrained to the W mass.

This example also illustrates one of the starting points of these lectures. As energies increase, the importance of good calorimetry increases since the resolution of this technique improves at higher energy. Also, the example shows that jets at high energy begin to take on the properties of particles and can be combined in ways in which we used to combine particles. Regardless of the details of the detector, its performance will depend on both the intrinsic strengths and weaknesses of the calorimeter technique as well as the implementation in a particular detector. Good design will require minimization of dead materials, optimization of detector thickness and sampling materials, consideration of compensation effects and careful planning for calibration. All of that, together with good software and a lot of hard work, will yield a calorimeter detector with great potential for doing interesting physics.

References

[1] Proc. Phy. Soc. A64 (1951) 511-512. "Deterioration of Anthracene under α-Particle Irradiation"

[2] W. Sippack et al. IEEE NS-36 (1989)

[3] M.G. Catanesi et al., NIM A260 (1987) 43-54

[4] G.A. Akopdjanov et al., NIM 140 (1977) 441-445

[5] E. Longo and I. Sestilli, NIM 128, 283 (1975)

[6] GEANT 3.10 Manual, PHYS 332-1 ff

[7] L. Landau, J. Phys. (USSR) 8 (1944), 201

[8] P.V. Vavilov, Soviet Physics, JETP 5 (1957), 749

[9] CERN Library G110, LANDAU

[10] CERN Library G111, DISVAV (Vavilov distribution)

[11] A.L. Sessoms et al., NIM 161 (1979) 371-382

[12] S. Bertolucci et al., NIM, A 254 (1987) 561

[13] C. Swenberg and N.E. Geacintov in Organic Molecular Photophysics (1973) Vol. 1

[14] ZEUS tests DESY 91-027

[15] DESY 90-100

[16] DESY 91-102

[17] R. Wigmans, NIM A259 (1987) 389

[18] R. Wigmans, NIM a 265 (1988) 273

[19] G.D'Agostini et al., NIM A274 (1989) 134-144

[20] T.A. Gabriel et al., ORNL/TM-11060 (1989)

[21] T.A. Gabriel et al., ORNL/TM-5619 (1977)

[22] T.A. Gabriel et al., NIM 195 (1982) 461-467

[23] M.B. Emmet, ORNL-49972 (1975)

[24] W.R. Nelson et al., SLAC-265 (1985)

[25] T.A. Gabriel, ORNL/TM-9727 (1985)

[26] P.A. Arnio et al., CERN, TIS-RP/168

[27] R. Brun et al., CERN DD/EE/84-1 (1986)

[28] J. del Peso and E. Ros DESY 91-005, Feb. 1991

[29] Y. Galaktionov et al., NIM A251 (1986) 258

[30] D. Groom SSC-227

[31] NIM, A 280 (1989) 36

[32] Hollebeek, Sinervo Snowmass '90

[33] H. Kowalski et al., DESY 87-170 (1987)